

# We are IntechOpen, the world's leading publisher of Open Access books Built by scientists, for scientists

6,900

Open access books available

186,000

International authors and editors

200M

Downloads

Our authors are among the

154

Countries delivered to

TOP 1%

most cited scientists

12.2%

Contributors from top 500 universities



WEB OF SCIENCE™

Selection of our books indexed in the Book Citation Index  
in Web of Science™ Core Collection (BKCI)

Interested in publishing with us?  
Contact [book.department@intechopen.com](mailto:book.department@intechopen.com)

Numbers displayed above are based on latest data collected.  
For more information visit [www.intechopen.com](http://www.intechopen.com)



# Application of 3D Simulation Methods to the Process of Induction Heating of Rail Turnouts

Elżbieta Szychta, Leszek Szychta, Mirosław Luft and Kamil Kiraga  
*Technical University of Radom, Institute of Transport Systems and Electrical Engineering  
 Poland*

## 1. Introduction

Keeping turnouts fully functional is necessary for safety of both train passengers and personnel operating railroads, particularly in winter. This is of particular importance since turnouts, key railroad elements, are exposed to adverse weather conditions. Proper function of turnouts is obstructed by snow falling between the point and the rail and between components of the setting lock which, combined with low ambient temperatures, causes the point to freeze to the sliding chairs and the components of the setting lock to freeze. This leads to blocking of a turnout<sup>1</sup>. Effective protection of turnouts against such weather conditions greatly reduces accident rates and improves efficiency of rail traffic.

The presented methods of heating railway turnouts all over the World are designed to prove operation efficiency turnouts during the winter. The authors set the goal of work to develop a new method of heating railway turnouts, using an inductive heating phenomenon. To do that it is necessary to know the properties of magnetic and electric rails. These properties are not explicitly specified by the manufacturers of rails, so the determination of their value by the laboratory tests is required. The chapter discusses the measurement methods used to determine the basic properties of electric and magnetic rails. Based on laboratory results a simulation model of inductive heating rails in 3D space is developed. In the final part of the chapter results of a simulation model tests are presented and discussed.

## 2. Contemporary methods of turnout heating

Methods of clearing snow and ice have evolved in line with the state of engineering art, weather conditions in a region as well as availability and costs of energy sources. The most common methods of heating turnouts in Europe include<sup>2</sup>:

- gas heating,
- water heating, used in smaller rail facilities, mainly in Germany. The first systems of this type in Poland were installed at Boguszów station,
- geothermal heating,

---

<sup>1</sup>Kiraga K., Szychta E., Andrulonis J. (2010). Wybrane metody ogrzewania rozjazdów kolejowych – artykuł przeglądowy

<sup>2</sup>Brodowski D., Andrulonis J. (2002). Ogrzewanie rozjazdów kolejowych, Problemy kolejnictwa

- electric heating by means of resistance heaters (most often supplied with 3X400 [V] systems, 230 [V] power supply, or with 15 [kV]  $16\frac{2}{3}$  [Hz] traction networks via voltage-reducing transformers).

Gas heating is used in extremely hard weather conditions (heavy snowfall and low temperatures of down to  $-30^{\circ}\text{C}$ ) on Austrian, Norwegian and Swiss railroads (the Alpine region) or in the Netherlands, where the weather is mild but very damp. Gas systems of turnout heating are characterised by high thermal efficiency. Gas burners reach power of up to 1000 [W/running metre of a rail]. Liquid mixtures of propane and butane or butane alone are most often employed as fuel. The gases display varied pressure depending on temperatures of condensed gas. The pressure reduces as the temperatures diminish. Mixtures of propane and butane are utilised where ambient temperatures are above  $-17^{\circ}\text{C}$ , replaced with butane itself below that temperature. Gas turnout heating is diagrammatically presented in Figure 1.

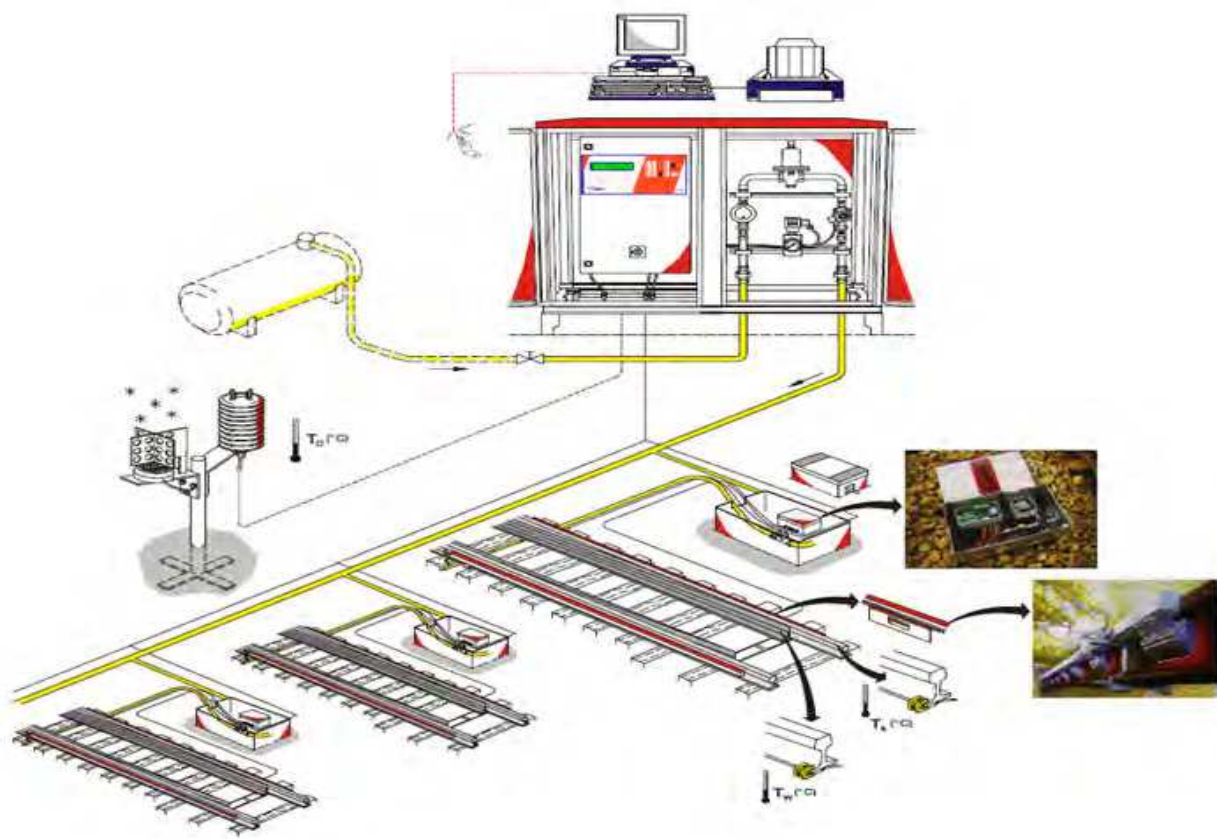


Fig. 1. Gas system of turnout heating

Water heating is another way of heating rail turnouts. An oil unit heats the working fluid, a mixture of water and anti-freeze agents. The heated fluid is supplied to pipe heat exchanges (heaters) which are fitted along a rail and turnout saddles. The fluid yields its heat and returns to the unit, cooled, to be re-heated. In a water heating system, the energy contained in the fuel (heating oil) is converted into heating power in the heating unit placed in the immediate vicinity of turnouts (normally in a building nearest to a signal cabin, which can itself be heated by the unit as well)<sup>3</sup>.

Design of a MAS water heating system comprises the following elements<sup>4</sup>:

- a heating station - including a heating unit, fuel tank, and a control system, 220V~/12V= (or 24V =) power supply to the heating unit, 12V (24V) battery as a reserve power source for the unit, and plumbing (surge tanks, pumps, pipes, cut-off valves),
- heating elements, i.e. heat exchangers inside a turnout,
- installation feeding the operating fluid from the heating station to turnouts.

Layout of a MAS system is shown in Figure 2.

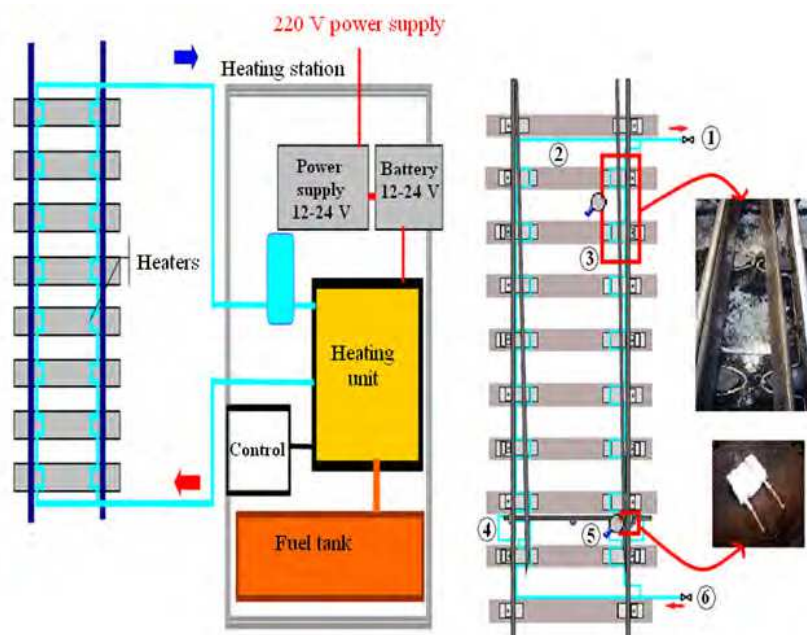


Fig. 2. Single-flow MAS water heating of a short turnout: 1 - return to unit, 2 - Ø 12mm steel pipe (heater), 3 - a heater located near a rail edge and sliding chair, 4 - heating of a setting lock, 5 - support heater, 6 - input

Geothermal systems are the third method of turnout heating discussed here. Geothermal heating, which uses the natural underground heat, is a new alternative to the systems presented above. A heat pump is its core element. Depending on the season and depth, soil temperatures may range from 4 to 8°C. At more than 15m below the ground level, season-related thermal motions cease and the temperature is constantly around 8-10°C. Still deeper, the soil is regenerated by flowing underground waters, heat from the earth's core and from above.

<sup>3</sup>Materiały seminaryjne CNTK. Wodne ogrzewanie rozjazdów kolejowych typu MAS

<sup>4</sup>Badania eksploatacyjne wodnego system ogrzewania rozjazdów typu MAS-Guben

Heat pumps operate like fridges which take advantage of the hot, not the cold section of the heat cycle. An appropriate working agent is compressed and decompressed producing a desired heating or cooling effect. To generate useful heat, for instance, soil or underground water heat (at low temperatures of approx.  $10^{\circ}\text{C}$ ) is employed to evaporate the operating agent (harmless gas R497C) that boils at a low temperature. Thus, the originally liquid working agent leaves an evaporator (heat exchanger on the side of ground collector) as gas. The gas is then compressed and condensated in a liquefier (heat exchanger on the side of heating installation) at high temperatures ( $50\text{--}60^{\circ}\text{C}$ ), yielding the condensation and compression heat to the water contained in the heating installation. The still pressurised working agent is subsequently decompressed in a valve and enters the low-pressure section, thereby initiating the cycle once again.

A complete system of geothermal turnout heating is illustrated in Figure 3.

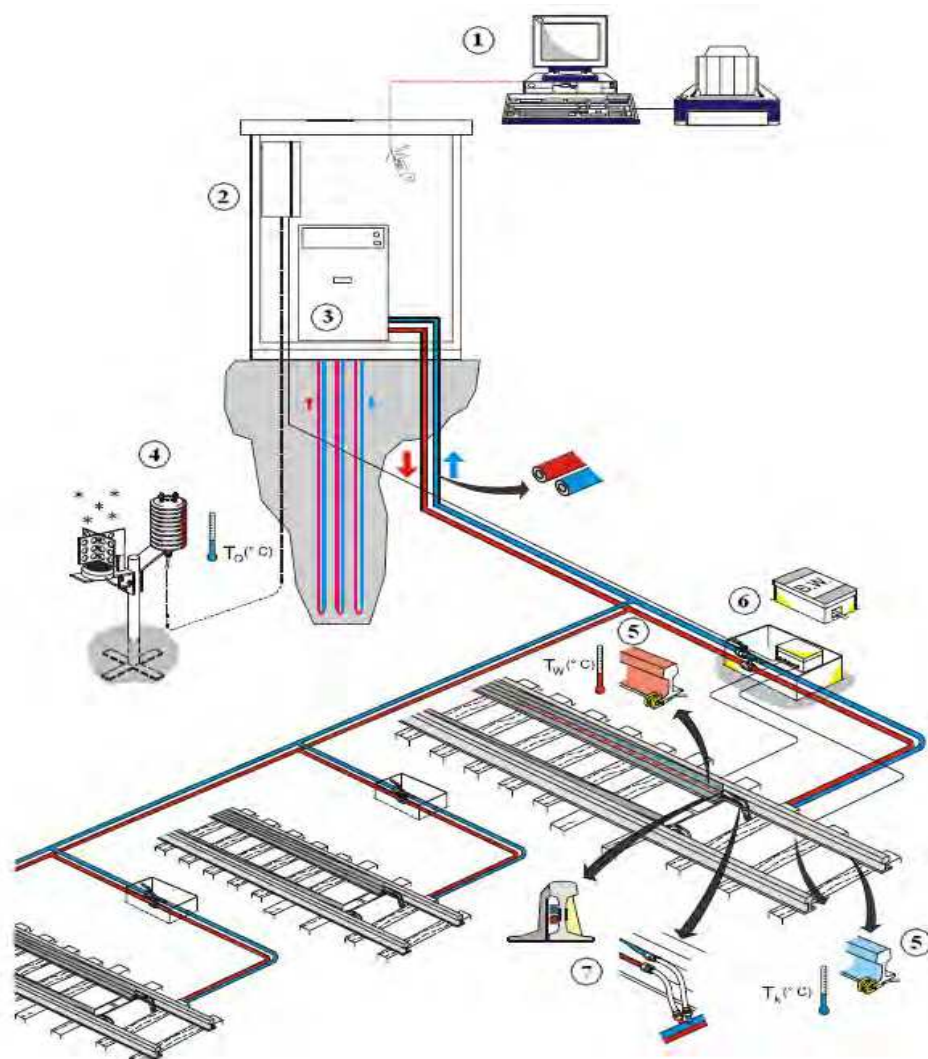


Fig. 3. Design of a geothermal turnout heating system including: 1 – a local control and monitoring system, 2 – an automatic control system containing an automatic weather unit, 3 – heat pump and heat cycle, 4 – snowfall and ambient temperature sensor, 5 – humidity and rail temperature sensors, 6 – junction box, 7 – heat exchangers (heaters) with heat-conducting insulation



Electric heating is the final method of turnout heating to be discussed here. The electric heating currently prevails in Poland among the equipment used to melt snow and ice on rail turnouts. It functions on more than 18 000 turnouts. Its combined installed power reaches approximately 110 [MW]<sup>5</sup>. The electric systems heat for an average of 300 hrs in a season. Providing 330W per running metre of rail assures effective warming of railroad turnouts during the heating season. The electric heating employing 330W/m heaters provides for good functioning of railroad turnouts under normal weather conditions (i.e. temperatures above -20°C) and with average (other than catastrophic) snowfall. A diagram of electric turnout heating is shown in Figure 4.

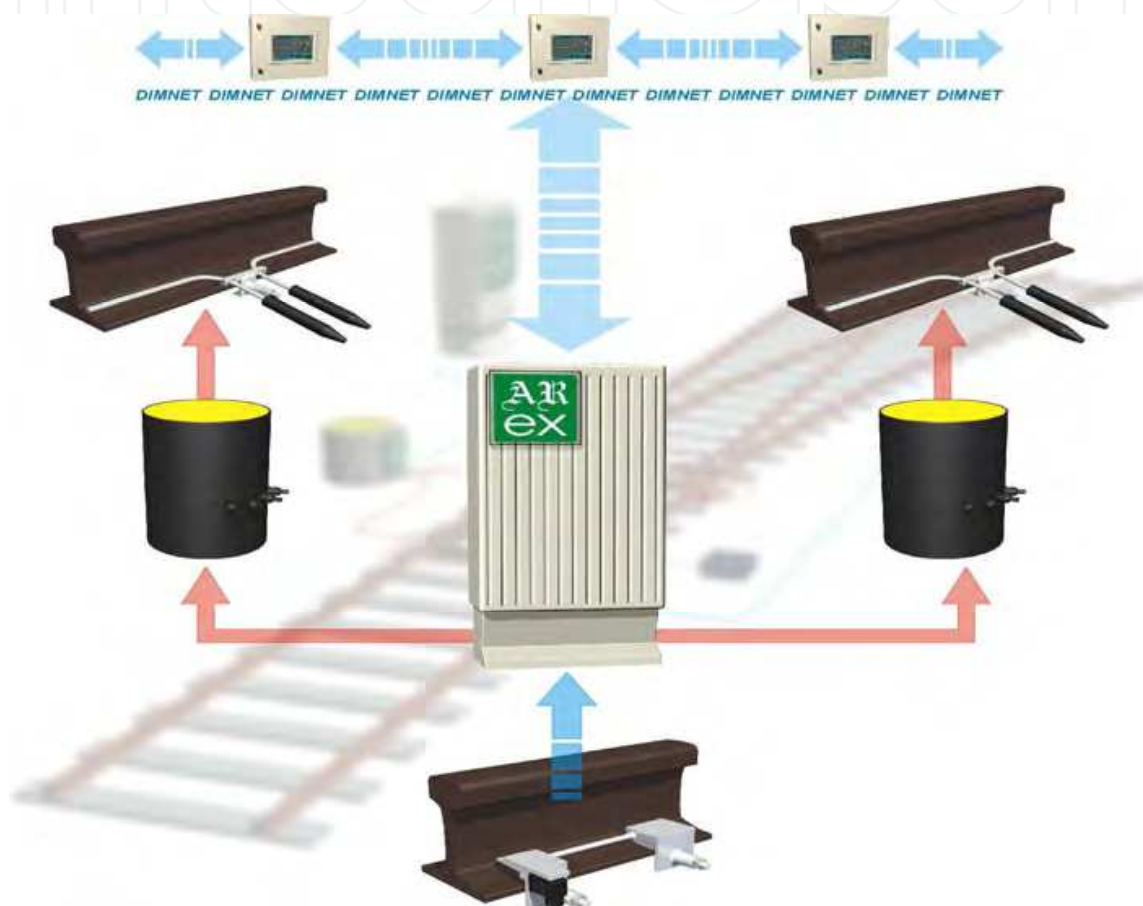


Fig. 4. Electric turnout heating

Recent years of cold winters and violent snowfalls have unfortunately shown that electric systems fail to provide effective heating of turnouts. The method of electric heating has therefore been modified to enhance its efficiency.

Performance trials are under way using heat insulation on Dutch, German, and Polish railroads. The rail foot is additionally insulated as part of these solutions. Arrangement of heat insulations on a rail is presented in Figure 5 below<sup>6</sup>.

<sup>5</sup>Brodowski D., Andrulonis J.(2000). Efektywność ogrzewania rozjazdów kolejowych

<sup>6</sup>Prospekt informacyjny o otulinach firmy Haet Point, 2009.

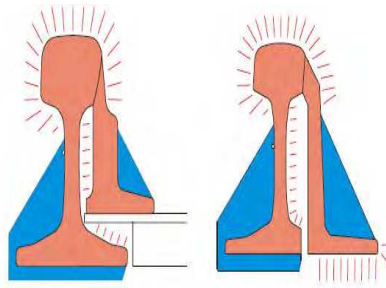


Fig. 5. Situation of insulations on the internal and external sides of a rail and on rail foot for every rail type

Such a solution is offered to PKP (Polish State Railroads) by Heat Point of the Netherlands, Research and testing will demonstrate potential advantages and drawbacks of this solution.

### 3. Induction heating of turnouts now and in the past

Induction turnout heating (an original Polish concept) was tested by PKP in 1978/1979 on selected turnouts and stations<sup>7</sup>. Insulated heating wires were used. They were not in galvanic contact with rails. Rails were heated with eddy currents induced inside the rails. The wires were heated to temperatures in the range  $+15^{\circ}\text{C}$  to  $+20^{\circ}\text{C}$ .

The heating wires were made of copper, wrapped with Tarflon tape, and placed inside a steel envelope. 3-3.3 [V] and 50 [Hz] were supplied to the wire, where the current was 350 [A].

The following types of heating wires were used:

- 2.55 [m], power 750 [W] for the rail UIC-49
- 3.00 [m], power 900 [W] for the rail UIC-60

A 2800 [VA] transformer was employed to supply power to each type of heaters. Given the mains frequency of 50 [Hz], the heating wires vibrated and produced human-audible acoustic waves whose frequency was twice greater than the frequency of the supplied voltage.

The inductive nature of power distribution system loading by iron equipment of the time required an additional capacitor to set off the reactive power and to improve the power factor  $\cos\phi$  from approx. 0.5 to 0.85 – 0.9. Capacitors capable of adjusting reactive power of 4 [kVA] or more were employed in a single given turnout. Work on the system and its application was abandoned due to insufficient technological resources at the time (1978/1979). The material on testing of inductive turnout heating discussed here is the only, scarce material still extant in the archives of the then COBiRTK (Centre for Rail Engineering Research and Development), currently named IK (Rail Engineering Institute).

These authors have decided to revive the idea of induction turnout heating and to use it, as part of a greater operating frequency system, to heat rail turnouts. A flow diagram of induction turnout heating as proposed by the authors is shown in Figure 6.

<sup>7</sup>Praca zbiorowe: Studium na temat wyboru optymalnego systemu ogrzewania rozjazdów

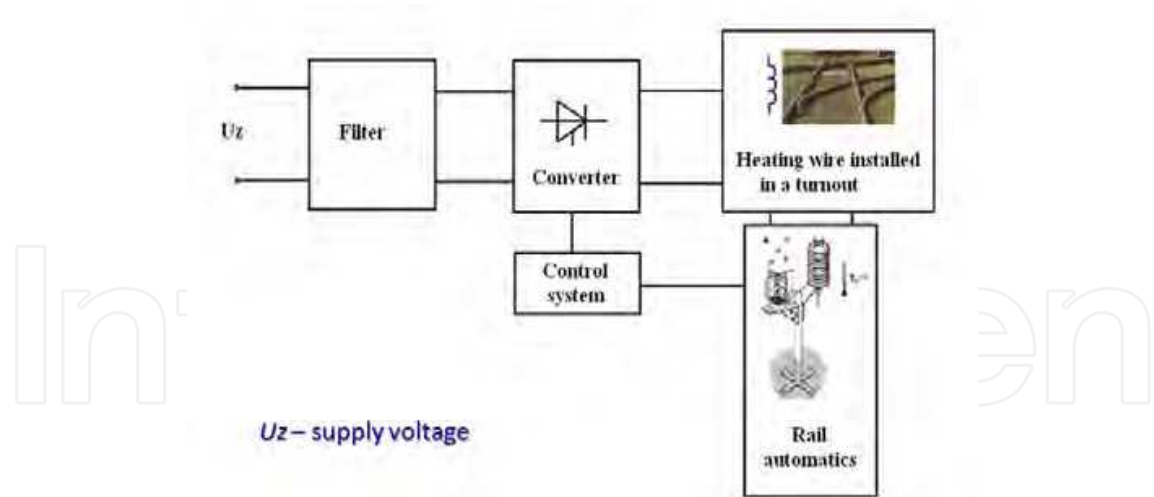


Fig. 6. System of induction turnout heating

Elementary theory concerning induction heating is not introduced as it is commonly known and easily available in engineering literature<sup>8 9</sup>. Knowledge of fundamental electric and magnetic properties of rails forming parts of turnouts is necessary to construct a fully functional induction heating system. Since not all of those properties are easily accessible or clearly defined, their values had to be determined experimentally by one of the methods described in the following section.

Attention focused then on the mathematical apparatus based on Maxwell’s equations and used to describe the electromagnetic field in space. Final element method (FEM) was subsequently discussed. Maxwell’s equations and FEM provide the foundations for an analytical model of induction turnout heating as executed in Flux 3D software.

4. Electric and magnetic properties of e160 rail

Rails (stock) are fundamental design elements of a turnout, beside switch points, sliding chairs or switching closure assemblies. Rails are principally designed to set the proper travel direction of rolling stock wheel sets. Shape of a rail comprises three characteristic sections: head (the part along which rolling stock wheels move), web, and foot (the part supporting the whole and carrying the load on to sleepers).

Two main rail types are used on routes administered by Polish State Railways PKP PLK: 60E1 and 49E1. They differ in the weight of a running metre and cross-section dimensions. 49E1 (49.39 kg/ running metre and cross-section surface area of 62.92 cm<sup>3</sup>) is used on routes with light rolling stock load. 60E1 (60.21 kg/ running metre and cross-section surface area of 76.70 cm<sup>3</sup>) is operated on heavily loaded routes where trains travel at speeds over 100 km/h.

Table 1 presents steel grades to be used in rail manufacture<sup>10 11</sup>. The grade references follow from applicable European and Polish standards (PN-EN 10027-1 and PN-EN10027-2). The

<sup>8</sup>Sajdak Cz., Samek E. (1985). Nagrzewanie indukcyjne. Podstawy teoretyczne i zastosowanie  
<sup>9</sup>Gozdecki T., Hering M., Łobodziński W. (1979). Urządzenia elektroniczne. Elektroniczne urządzenia grzejne  
<sup>10</sup>Wielgosz R. (2009). Łączenie bezстыkowych szyn kolejowych



symbols of rail materials are based on rolling surface hardness, in Brinell degrees, with the added symbol of an element used to refine the rail steel or in reinforcement heat treatment. Table 1 also includes references to previously used steel grades, of chemical compositions similar to the new steels recommended by the EU in accordance with EN 13674-1:2003 (E).

Two steel grades most commonly used in Poland are R260 (hardness range 260÷300 HB) and R350HT (hardness range 350÷390 HB, heat treated head).

| Steel marking | Description                   | Material number | Previous marking |
|---------------|-------------------------------|-----------------|------------------|
| R200          | Carbon-manganese              | 1.0521          | R0700            |
| R220          | Carbon-manganese              | 1.0524          | R0800            |
| R260          | Carbon-manganese              | 1.0623          | R0900; St90PA    |
| R260Mn        | Carbon-manganese              | 1.0624          | R0900Mn; St90PB  |
| R320Cr        | Low alloy                     | 1.0915          | R1100Cr          |
| R350HT        | Heat treated carbon-manganese | 1.0631          | R1200            |
| R350LHT       | Heat treated low alloy        | 1.0632          |                  |

Table 1. Rail steel markings

The steels formerly used in rails contain 0.40 to 0.82% carbon, 0.60 to 1.70% manganese, 0.05 to 0.90% silica, and some additionally contain up to 1.30% chromium. The new steels recommended by the EU contain: 0.38 - 0.82% carbon, 0.65 - 1.70% manganese, 0.13 - 1.12% silica, and some additionally contain up to 1.25% chromium.

As steel is heated and cooled and temperatures change in rail manufacturing processes, structural transformations occur. In the final production process, a rail is hot rolled at temperatures of 700 – 900°C. The (heterogeneous) structure and material properties of the rail result from such processes.

60E1 is selected for purposes of testing electric and magnetic properties because it serves trans which travel at up to 100 km/h. Standardised dimensions of normal-gauge 60E1<sup>12 13</sup> are illustrated in Figure 7.

The following elements of a heating circuit are analysed as part of testing aimed at developing a method of induction turnout heating: structure of rail material, resistivity and magnetic permeability, skin effect and depth of magnetic field penetration into the rail structure, discharge of active power in the form of impact of the magnetic field on the rail. These parameters depend, inter alia, on magnetising current frequency and are not defined by rail manufacturers. It appears rails may come from different charges, may be produced by means of diverse rolling, straightening, and possibly hardening technologies. It was therefore important to determine locations from which rail samples would be removed. To generate a maximum quantity of data for further research, samples were withdrawn (cut) from key points of a rail. Sample removal locations and their geometric dimensions are shown in Figure 8.

<sup>11</sup>strona internetowa odnośnie szyn kolejowych: [www.inzynieria-kolejowa.dl.pl](http://www.inzynieria-kolejowa.dl.pl)  
<sup>12</sup>Grobelny M. (2009) Budowa, modernizacja, naprawa i remonty nawierzchni kolejowej – urządzenia i elementy  
<sup>13</sup>Instrukcja eksploatacji i utrzymania urządzeń elektrycznego ogrzewania rozjazdów

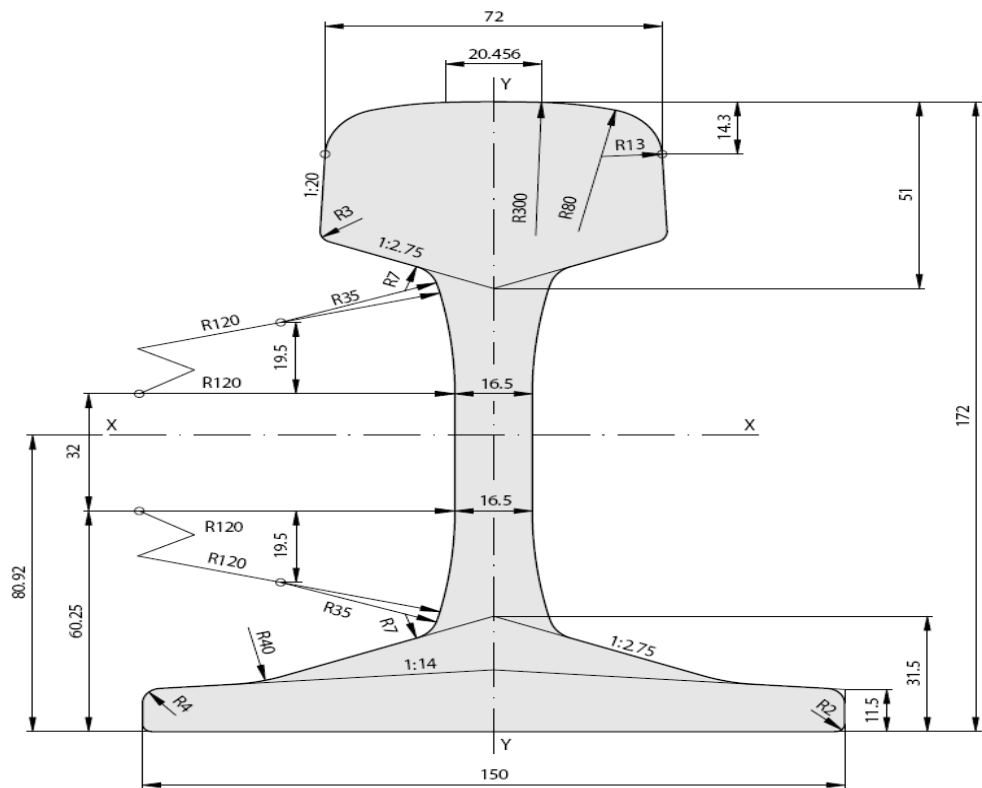


Fig. 7. Geometrical dimensions of the normal-gauge E160

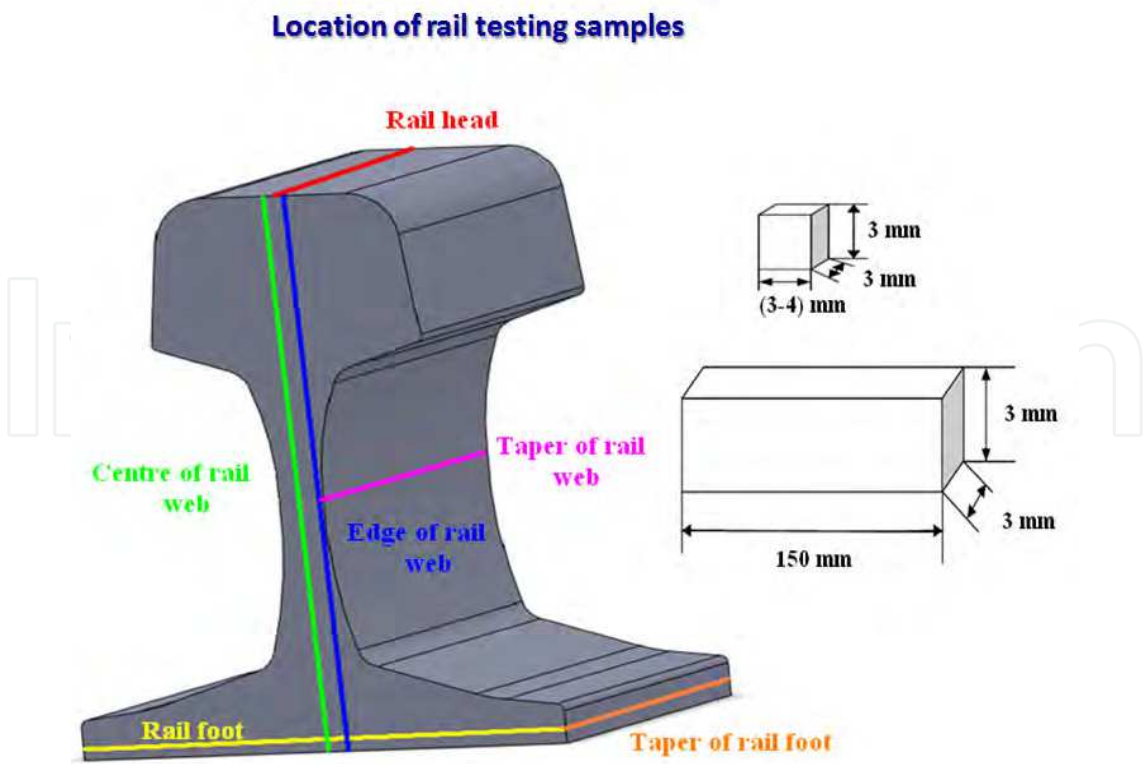


Fig. 8. 60E1 sample removal locations and their geometric dimensions

Determining key electric and magnetic parameters of construction materials for railroad turnouts was essential in designing a system of induction heating and employed a variety of testing methods. Electric and magnetic parameters were determined by means of the following methods:

- *four-point linear probe method* to determine electric resistivity (taken into consideration as rotary currents arise when the magnetic field penetrates the internal structure of a rail).

A flow diagram of electric resistivity measurements is illustrated in Figure 9.

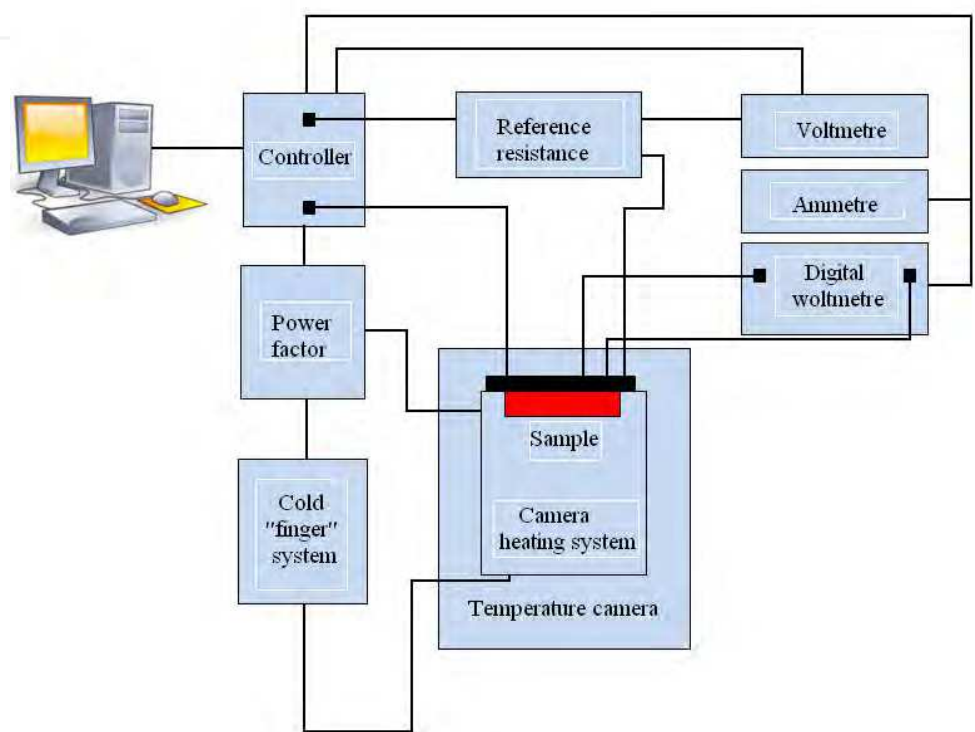


Fig. 9. Flow diagram of electric resistivity measurement system

Electric resistivity can be measured by means of a four-point linear probe and a measurement system which employs a PC to record the voltage drop across a tested sample and across a reference resistor  $R_w$ . Voltage is checked by running the current (10 times) in two directions. Once averaged, both the results are added and contact effects are eliminated in this way. The result is averaged and saved to the memory. The current's value can be calculated according to:

$$I_x = \frac{U_{Rw}}{R_w} \tag{1}$$

With known geometric dimensions of the sample, that is, its height  $a$  and width  $b$ , electric resistivity can be determined on the basis of:

$$\rho = \frac{U_x}{I_x} \cdot \frac{S}{l} = R_{mierz} \cdot \frac{S}{l} \tag{2}$$

where:

- $U_x$  – voltage drop across the sample,
- $I_x$  – measurement current,
- $S$  – cross-section of the sample,
- $l$  – distance between the measurement probes.

Table 2 summarises results of electric resistivity measurements for samples from characteristic rail locations.

| Source of the sample | Mean electric resistivity $\rho$ [ $\Omega\text{m}$ ] |
|----------------------|---|
| Edge of rail web     | $2.62 \cdot 10^{-7}$                                  |
| Centre of rail web   | $2.85 \cdot 10^{-7}$                                  |
| Rail foot            | $2.75 \cdot 10^{-7}$                                  |
| Taper of rail foot   | $2.57 \cdot 10^{-7}$                                  |
| Taper of rail web    | $2.7 \cdot 10^{-7}$                                   |
| Rail head            | $2.58 \cdot 10^{-7}$                                  |

Table 2. Values of electric resistivity for the tested samples

- *HP bridge*: active and passive magnetic hardness as well as the loss tangent are determined. Initial magnetic hardness can also be defined since the intensity of the magnetic field is low.

Hewlett Packard 4284A 20Hz – 1MHz Precision LCR Meter helps to conduct measurements in order to determine relative magnetic permeability  $\mu$  of selected rail sections.

A connection link is replaced with a measurement coil of known length  $l$  and number of coils  $z$ . A sample is placed inside the coil. The bridge circuit is supplied with AC. A millivoltmetre of very high internal resistance is connected in parallel to the coils with the sample inside. It can measure the voltage drop across this element and, consequently, select the magnetising field as appropriate. The device also provides for de-magnetising of samples using a 50Hz field whose amplitude reduces towards zero, for regulation and stabilisation of temperature.

The system used to determine relative magnetic permeability  $\mu$  of the tested rail sections consisted of:

- a PC and its software,
- Aligent 34401A 6 ½ Digital Multimeter,
- (hp) Hewlett Packard 4284A 20Hz – 1MHz Precision LCR Meter,
- and a measurement coil.

Figure 10 contains a diagram of the measurement stand serving to determine  $\mu$ .

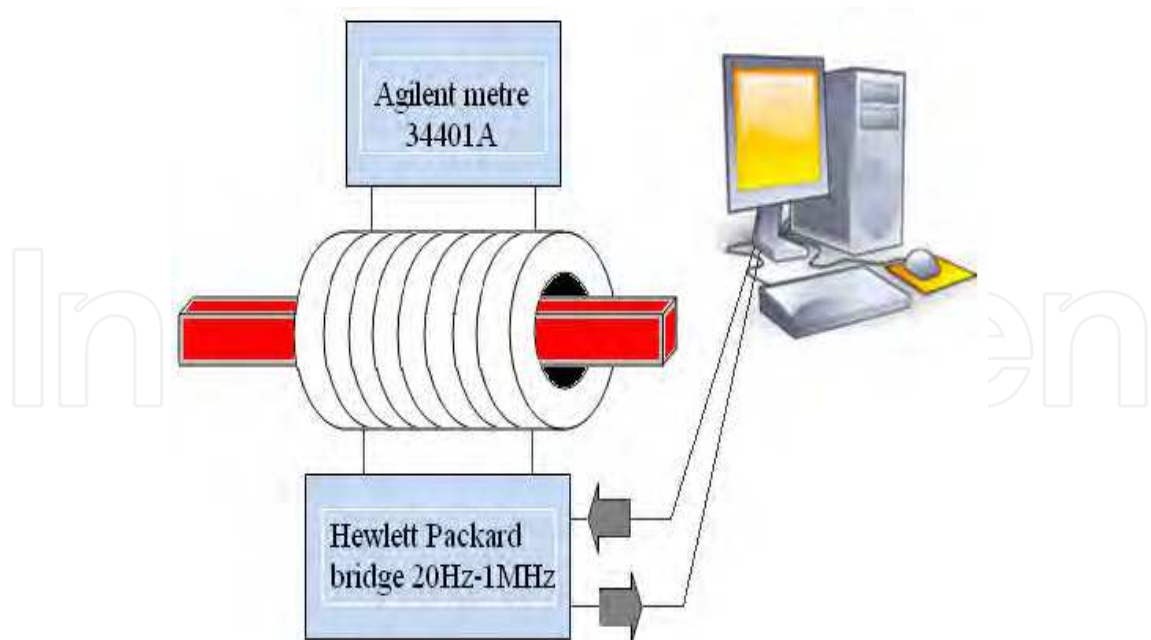


Fig. 10. Measurement apparatus serving to determine relative magnetic permeability  $\mu$

An AC bridge is the chief component of the system which provides for accurate measurement of combined magnetic permeability:

$$\underline{\mu} = \mu_{cz} + i\mu_b \tag{3}$$

The combined permeability comprises:

- the component active magnetic permeability  $\mu_{cz}$  responsible for magnetising processes,
- the component passive magnetic permeability  $\mu_b$  responsible for magnetic losses.

The active magnetic permeability can be formulated:

$$\mu_{cz} = \frac{(L_x - L_0) \cdot l}{\mu_0 z^2 S_p} + 1 \tag{4}$$

here:

- $L_x$  – inductivity of the coil containing the sample,
- $L_0$  – inductivity of an empty coil,
- $\mu_0$  – magnetic permeability of the vacuum  $\mu_0 = 4\pi \cdot 10^{-7} \text{H/m}$ ,
- $S_p$  – cross-sectional surface area of the tested sample,
- $z$  – number of coils,
- $l$  – length of the coil.

As  $\mu_{cz} \gg 1$ , 1 is ignored in the calculations.

The passive magnetic permeability is computed:

$$\mu_b = \frac{R_{rdz} \cdot l}{\mu_0 \cdot Z^2 \cdot 2\pi \cdot f \cdot S_p} \tag{5}$$



$R_{rdz}$ , or the core's resistance, is calculated:

$$R_{rdz} = R - R_0 \tag{6}$$

where:

$R_0$  – resistance of an empty coil,  
 $R$  – resistance of the coil containing the sample.

Substituting (6) to (5) produces the following equation of passive magnetic permeability:

$$\mu_b = \frac{R_{rdz} \cdot l}{\mu_0 Z^2 2\pi f S} = \frac{(R - R_0) \cdot l}{\mu_0 Z^2 2\pi f S} \tag{7}$$

Measuring voltage drop across the resistance  $R$  helps to determine intensity of the electric current across the winding and then the intensity of the magnetic field at which magnetic permeability is measured using the dependence:

$$H = \frac{Z \cdot U}{l \cdot R} \tag{8}$$

where:

$z$  – number of coils,  
 $U$  – voltage drop across the resistor  $R$ ,  
 $l$  – length of the measurement coil.

Figure 11 illustrates the initial magnetic permeability  $\mu_{initial}=f(f)$  of a sample from the rail web edge (red) and  $\mu_{initial} = f(f)$  of a sample from the rail's head (black) as well from the rail's core (the green curve).

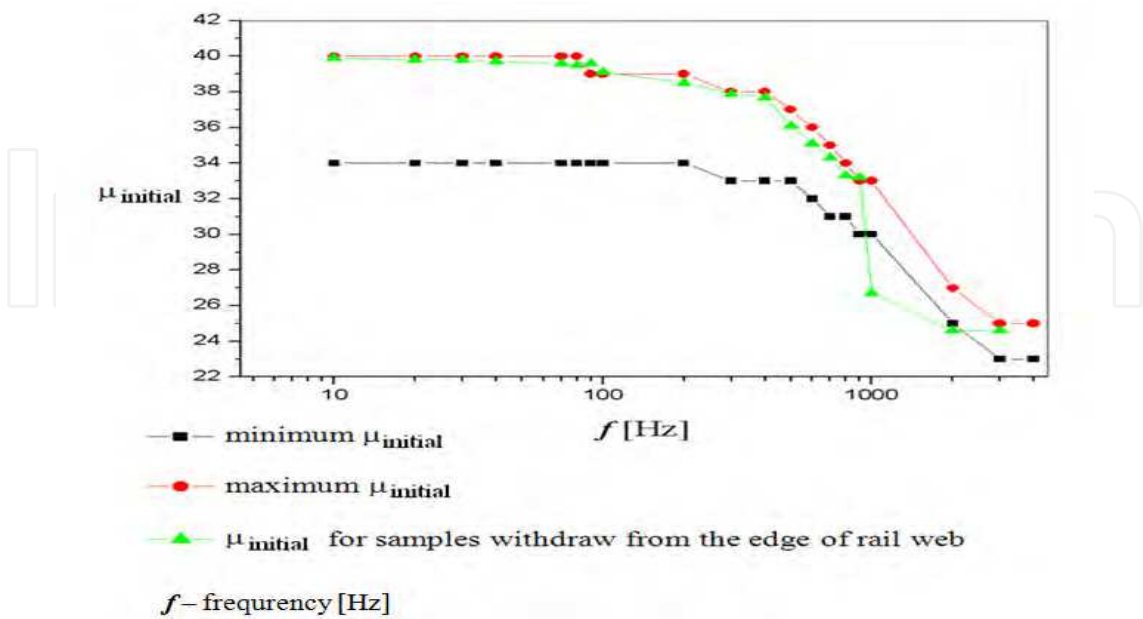


Fig. 11. Magnetic permeability  $\mu_{initial}=f(f)$  for a sample from the edge of rail web and  $\mu_{initial} = f(f)$  for the remaining samples.

- A *fluxmetre* serves to plot the curves  $B = f(H)$  and  $\mu = f(H)$ <sup>14 15</sup>,

Prime magnetising curves were determined by means of the measurement system shown in Figure 12.

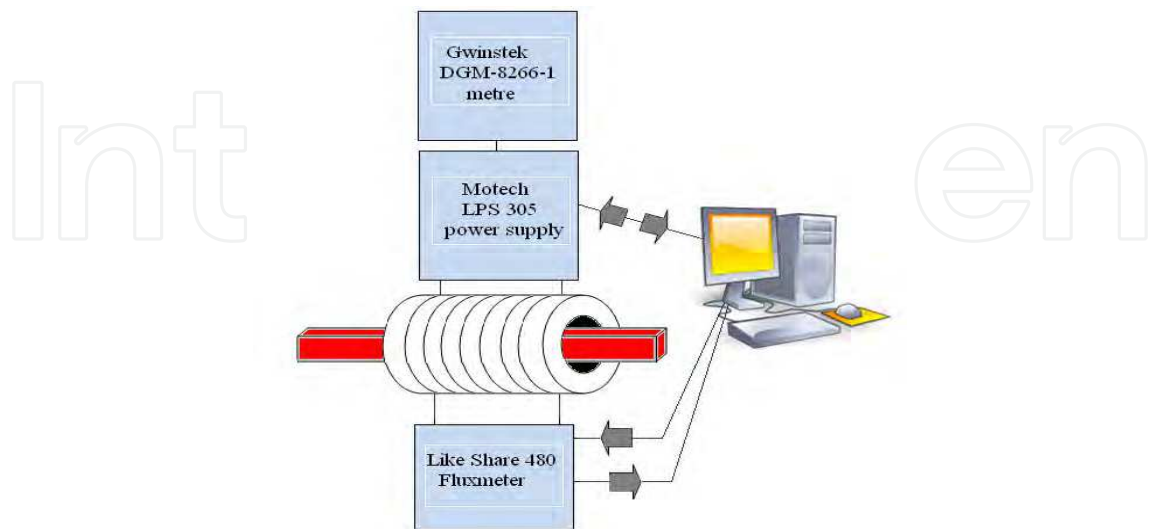


Fig. 12. Measurement system employing the fluxmetre and its components

The tested sample is placed inside the coil in magnetising and measurement winding. A fluxmetre to measure magnetic flow variations in the tested material sample is the element of the measurement system. Variations in the tested material sample result from commutations of the current across the magnetising winding  $z_m$ . The electric current pulse induced in the measurement winding over time  $dt$  is measured by the fluxmetre. The magnetic flow variations  $d\Phi$  generate an electromotor force  $\varepsilon$  which can be expressed:

$$\varepsilon = -\frac{d\phi_c}{dt} = -z_p \cdot \frac{d\phi}{dt} \tag{9}$$

Fluxmetre readings are proportional to magnetic flow variations.

When a uniform external magnetic field is applied, magnetic induction  $B$  can be computed according to:

$$B = \frac{d\phi}{2z_p S} \tag{10}$$

where  $S$  is the cross-sectional surface area of the tested sample. The sample is demagnetised prior to each measurement by means of the system.

A prime magnetising curve for a sample from the rail web and maximum magnetic permeability in respect of the same sample determined using the fluxmetre are shown in Figure 13.

<sup>14</sup>Gignoux D., Schlenker M.(2005). *Magnetism Fundamentals*  
<sup>15</sup>Jiles D. (1991). *Introduction to Magnetism and Magnetic Materials*

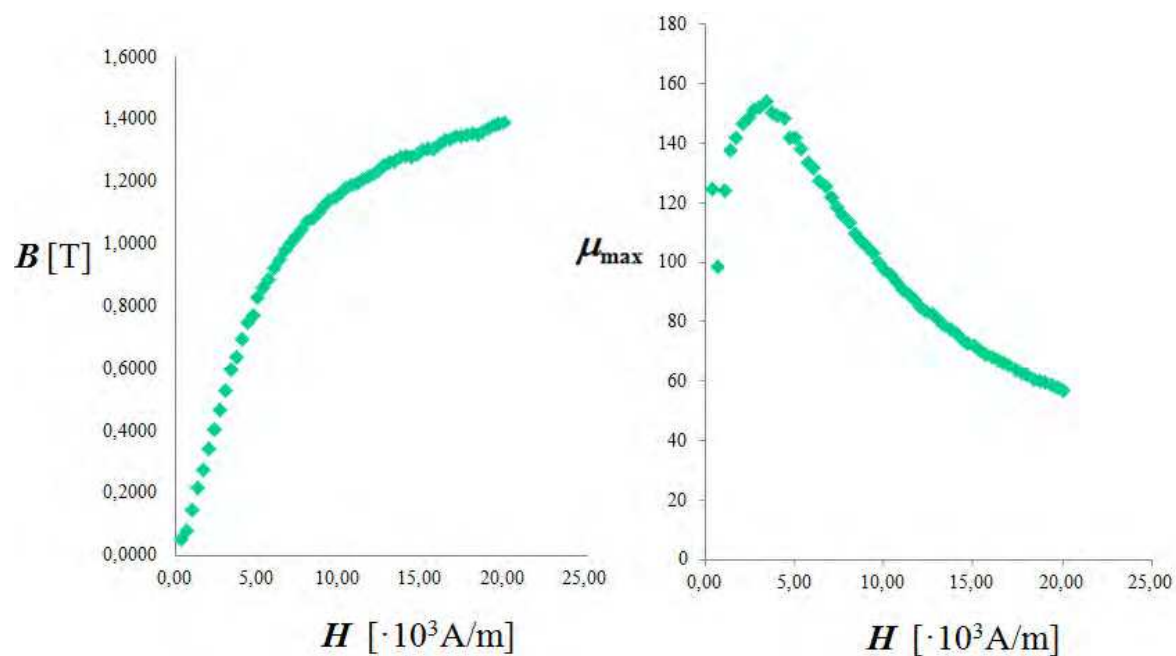


Fig. 13. Curves  $B = f(H)$  and  $\mu = f(H)$  for a sample of the rail web

- *coercion metre* measures intensity of the coercion field,

Intensity of the coercion field of magnetically soft and hard materials can be measured by means of a coercion metre. The relevant measurement diagram is presented in Figure 14.

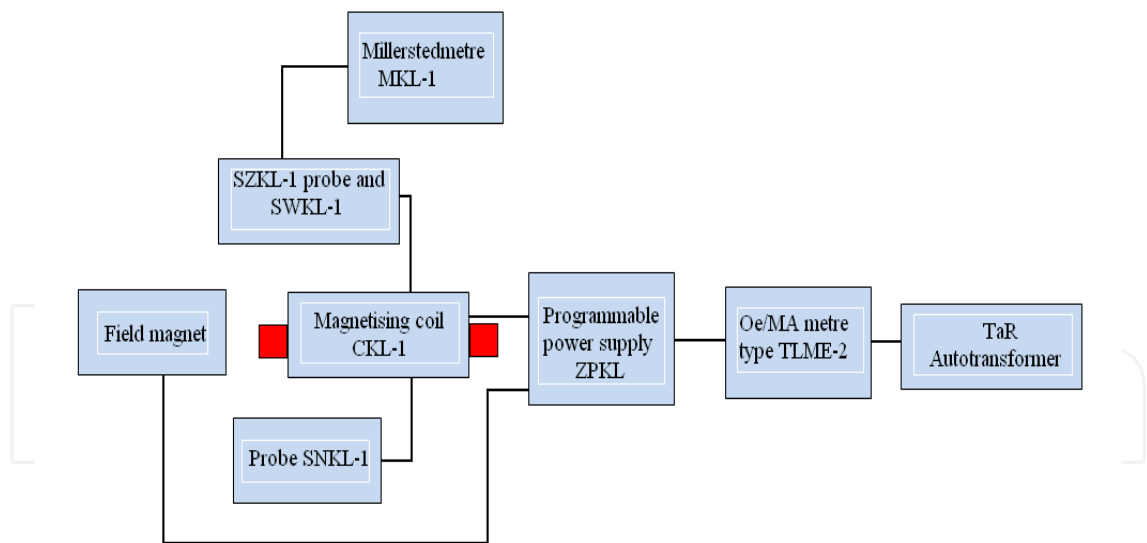


Fig. 14. Measurement diagram using a coercion metre and its components

Magnetic coercion<sup>16</sup> (also referred to as coercive force) is the value of an external magnetic field that must be applied to a material (e.g. a ferromagnetic material) to bring the magnetic residue down to zero. The magnetic residue (also remanence or residual magnetisation) is the magnetic induction remaining after an external magnetic field magnetising a given material is removed.

<sup>16</sup>Kuryłowicz J. (1962). Badania materiałów magnetycznych

Table 3 summarises measurement results of magnetic coercion intensity for samples removed from key rail locations.

| Source of the sample | Sample number | Hc [A/m] | Mean Hc [A/m] |
|----------------------|---------------|----------|---------------|
| Edge of rail web     | 1             | 820      | 823           |
|                      | 2             | 820      |               |
|                      | 3             | 828      |               |
| Centre of rail web   | 1             | 772      | 774           |
|                      | 2             | 776      |               |
|                      | 3             | 772      |               |
| Rail foot            | 1             | 772      | 778           |
|                      | 2             | 772      |               |
|                      | 3             | 788      |               |
| Taper of rail foot   | 1             | 876      | 912           |
|                      | 2             | 884      |               |
|                      | 3             | 1003     |               |
|                      | 4             | 884      |               |
| Taper of rail web    | 1             | 860      | 830           |
|                      | 2             | 860      |               |
|                      | 3             | 804      |               |
|                      | 4             | 796      |               |
| Rail head            | 1             | 812      | 850           |
|                      | 2             | 860      |               |
|                      | 3             | 820      |               |
|                      | 4             | 908      |               |

Table 3. Coercion field intensity in respect of all samples

- PPMS VSM was utilised to plot the curve  $J = f(H)$ ,

A Physical Property Measurement System (PPMS) by Quantum Design (San Diego, USA) is a unique, state-of-the-art concept of a laboratory facility.

The PPMS platform comprises the following elements:

- superconducting magnet of up to 7 Tesla (and, more recently, even 16 Tesla),
- specific heat measurement system (Heat Capacity 4He) in the temperature range 2K – 400K and magnetic fields of up to 7 Tesla,
- specific heat measurement system (Helium-3) in the temperature range 350mK – 350K and magnetic fields of up to 7 Tesla,
- AC/DC magnetisation measurement system for magnetic fields of up to 7 Tesla,
- vibration magnetometer VSM for precise magnetising measurements In a broad temperature range of 2K to 1000K. It is additionally fitted with an oven (P527 Sample Magnetometer Oven) for measurements of up to 1000K.
- heat conductivity and thermal force measurement system,

- measurement capability of electric resistance in the range of 350mK,
- vertical rotator to regulate sample position in relation to the magnetic field,
- and an easyLab Pcell 30kbar pressure chamber to measure resistance at high pressure of up to 30kbar.

The overall flow diagram of PPMS platform is shown in Figure 15.

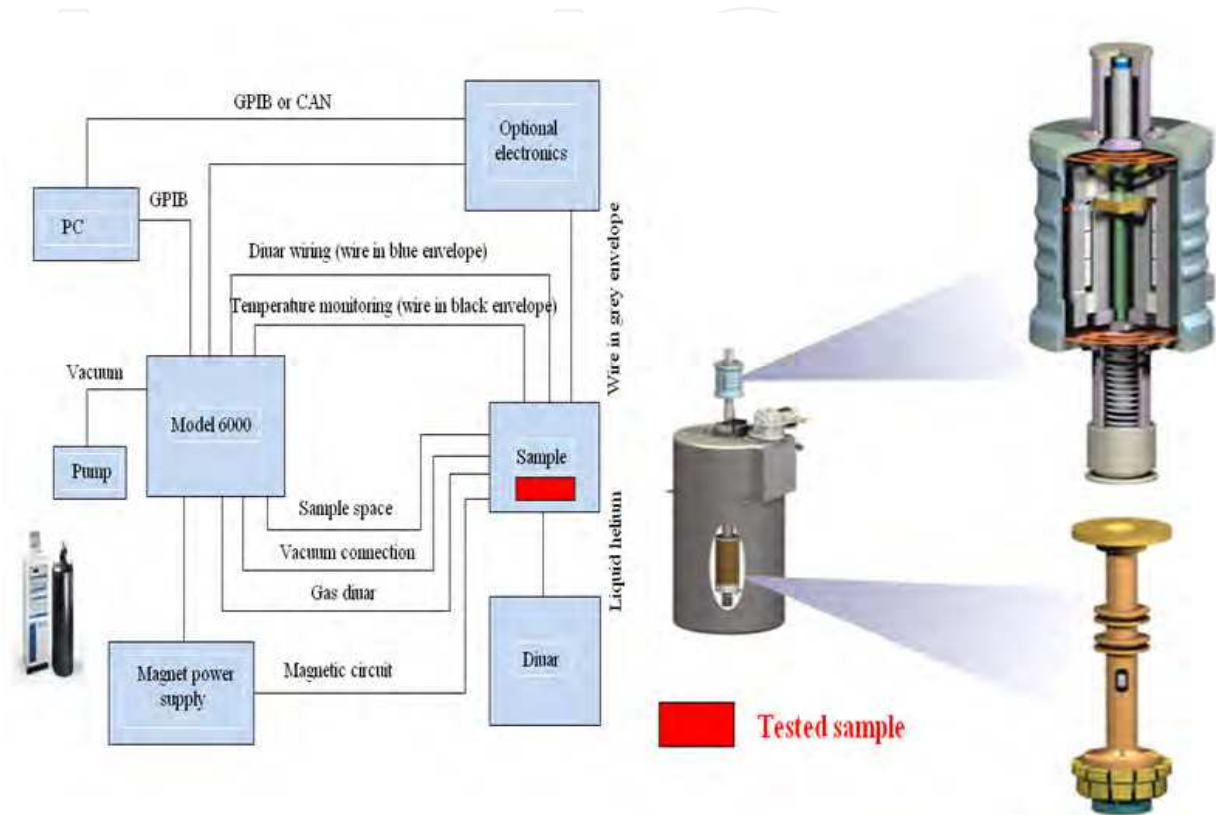


Fig. 15. Physical Property Measurement System to test magnetic properties of rail samples

A magnetometer suction cup with the vibrating sample was employed to plot prime magnetising curves and to determine saturation of the tested rail samples.

A sample is positioned on a non-magnetic, mobile bar and vibrates vertically at a set frequency. The sample’s oscillations generate (induce) a variable voltage signal in the measurement coil system under impact of the magnetic field. The signal is proportional to the magnetic moment of the sample and to parameters characterising its motion, i.e. to the amplitude and vibration frequency. It can be described as follows:

$$V_{cewki} = -\frac{d\phi}{dt} = -\left(\frac{d\phi}{dz}\right)\left(\frac{dz}{dt}\right) = C\ m\ A\ \omega\ \sin\ (\omega\ t)$$

(11)

where:

- C -proportionality constant,
- m – a known moment of the sample,
- A – vibration (oscillation)amplitude,
- ω – frequency.



A flow diagram of vibrating sample magnetometer (VSM) is illustrated in Figure 16.

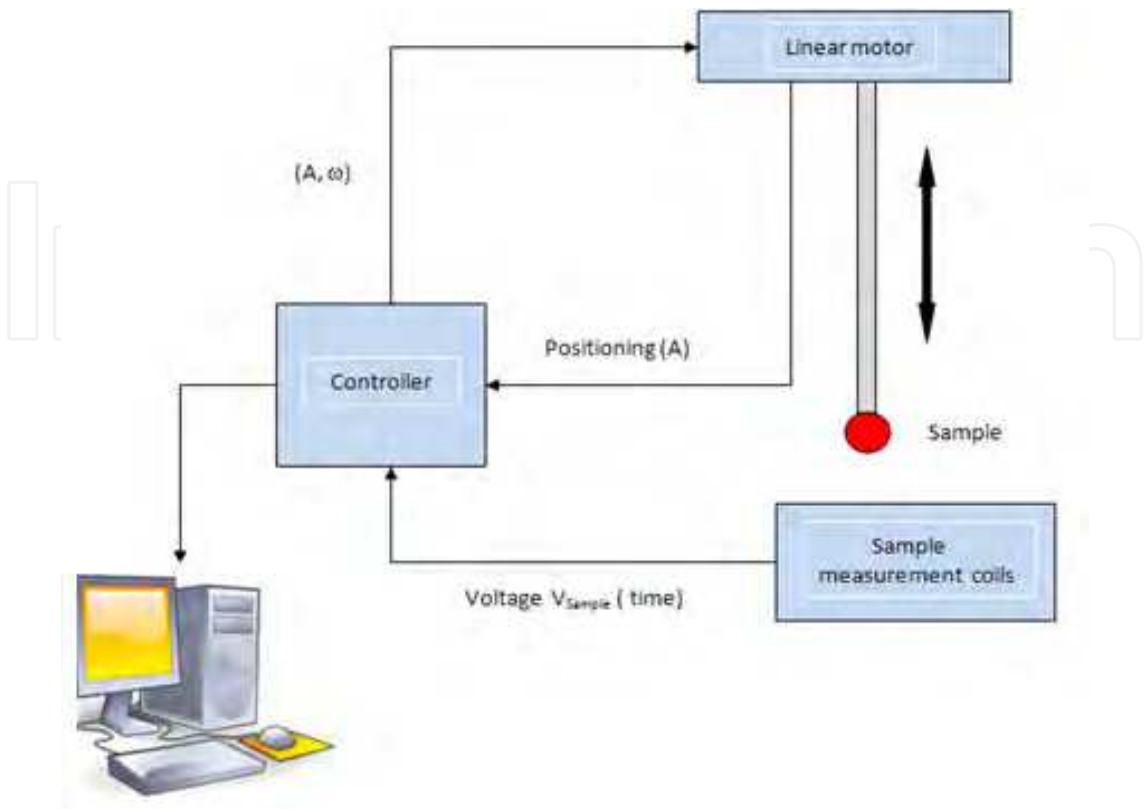


Fig. 16. Flow diagram of VSM measurement platform

Figure 17 presents a magnetising curve  $J = f(H)$  and magnetic saturation  $J_s$  for rail head samples.

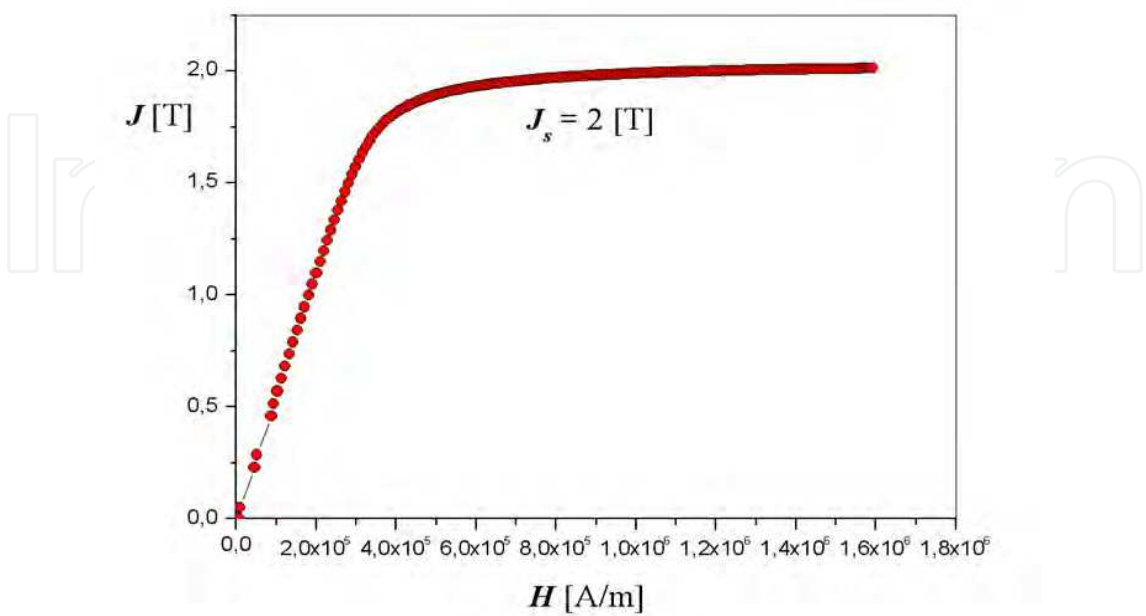


Fig. 17. Magnetising curve  $J = f(H)$  and magnetic saturation  $J_s$  for rail head samples

- ACMS determines combined magnetic susceptibility, including its real and imaginary components, the loss tangent for varied intensities of the magnetic field and for different temperatures.

ACMS (AC Measurement System) provides for a single sequence of measurements of AC and DC susceptibility in a broad temperature range from 1.9K – 350K. AC measurements are thrice as sensitive ( $2 \times 10^{-8} \text{emu}$  ( $2 \times 10^{-11} \text{Am}^2$ ) at 10kHz) as DC measurements. Better results may be occasionally obtained by means of the DC method. Application of a powerful external field can increase the sample's magnetic moment and generate signals above the noise (the range of DC magnetising DC:  $2.5 \times 10^{-8} \text{Am}^2$  -  $5 \times 10^{-3} \text{Am}^2$  ( $2.5 \times 10^{-5} \text{emu}$  -  $5 \text{emu}$ )). DC measurement uses a constant field in the measurement area where the sample moves by means of detection coils and induces voltage there according to Faraday's law. Amplitude of this signal depends on the sample's magnetic moment and the rate of its removal. As part of this system, the sample is extracted at an approximate speed of 100cm/s. The signal's force grows considerably as a result compared to other systems. The measurements can be executed as a function of both temperature and of the magnetic field.

Flow diagram of ACMS and its key elements are shown in Figure 18.

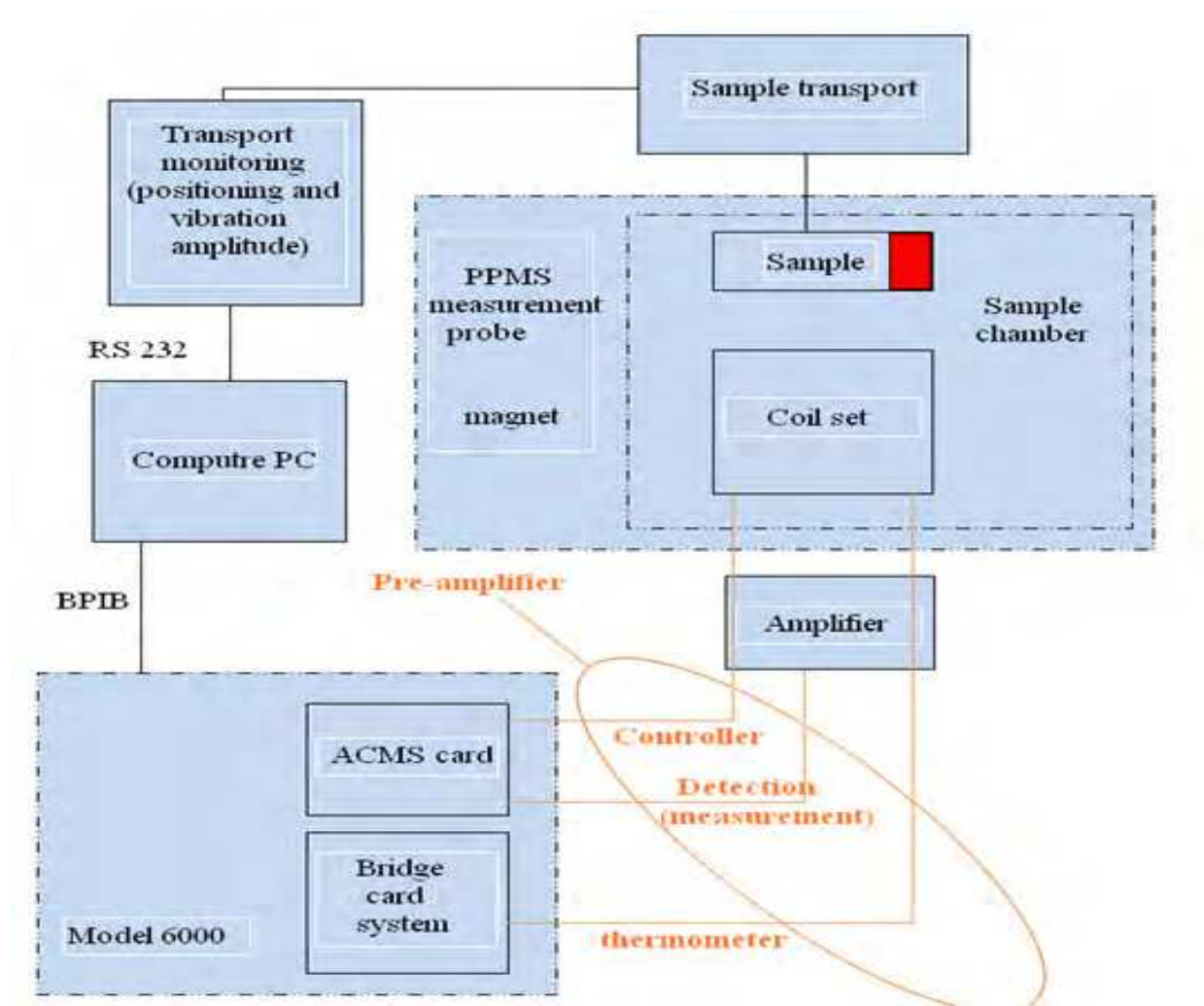


Fig. 18. Flow diagram of ACMS

Table 4 summarises loss factors on eddy currents and magnetic hysteresis for samples collected in key rail locations determined at varied temperatures by means of ACMS platform.

| Source of the sample | Temperature [°C] | Loss factor on eddy currents $w$ [ $10^{-4}$ s] | Loss factor on magnetic hysteresis loop [ $10^{-5}$ m/A] |
|----------------------|------------------|---|--|
| Edge of rail web     | 0 [°C]           | 2.49  | 2.31   |
|                      | 25 [°C]          | 2.33  | 2.62   |
|                      | -25 [°C]         | 2.7   | 2.44   |
| Centre of rail web   | 0 [°C]           | 2.53  | 2.42   |
|                      | 25 [°C]          | 2.33  | 2.8  |
|                      | -25 [°C]         | 2.72  | 2.78   |
| Rail foot            | 0 [°C]           | 2.31  | 1.42   |
|                      | 25 [°C]          | 2.13  | 1.45   |
|                      | -25 [°C]         | 2.49  | 1.63   |
| Taper of rail foot   | 0 [°C]           | 2.39  | 1.94   |
|                      | 25 [°C]          | 2.2   | 1.97   |
|                      | -25 [°C]         | 2.6   | 1.77   |
| Taper of rail web    | 0 [°C]           | 1.83  | 1.55   |
|                      | 25 [°C]          | 1.69  | 1.76   |
|                      | -25 [°C]         | 2.56  | 1.83   |
| Rail head            | 0 [°C]           | 2.62  | 2.49   |
|                      | 25 [°C]          | 2.42  | 2.4  |
|                      | -25 [°C]         | 2.83  | 2.68   |

Table 4. Loss factors on eddy currents and magnetic hysteresis

A 3D simulation model of induction turnout heating was constructed in FLUX 3D software on the basis of 60E1 rail’s electric and magnetic parameters discussed above.

5. Issues relating to spatial descriptions of magnetic field

Beside the foregoing electric and magnetic parameters, a magnetic field description in three-dimensional space by means of scalar magnetic potential, finite elements method (FEM), and normalised geometric dimensions of 60E1 (Fig. 7) served to construct a 3D simulation model of induction turnout heating. The magnetic field description by means of scalar magnetic potential and finite element method will be explained in detail below

In a non-linear environment, the electromagnetic field at any type of input function is described with Maxwell’s equations which relate intensities of the magnetic field, electric field, and charge as parts of the following differential dependencies (12 – 15):

$$\nabla \times \underline{H} = \underline{J} + \frac{\partial \underline{D}}{\partial t} \quad (12)$$

$$\nabla \times \underline{E} = - \frac{\partial \underline{B}}{\partial t} \quad (13)$$

$$\nabla \cdot \underline{B} = 0 \quad (14)$$

$$\nabla \cdot \underline{D} = \rho \quad (15)$$

Maxwell's equations are integrated into:

$$\oint_l \underline{H} \cdot d\underline{l} = \int_s \underline{J} \cdot d\underline{S} + \frac{\partial}{\partial t} \int_s \underline{D} \cdot d\underline{S} \quad (16)$$

$$\oint_l \underline{E} \cdot d\underline{l} = - \frac{\partial}{\partial t} \int_s \underline{B} \cdot d\underline{S} \quad (17)$$

$$\int_s \underline{B} \cdot d\underline{S} = 0 \quad (18)$$

$$\int_s \underline{D} \cdot d\underline{S} = \int_v \rho dV \quad (19)$$

Maxwell's equations are complimented with the material dependences:

$$\underline{B} \equiv \underline{B}(\underline{H}) \quad (20)$$

$$\underline{D} \equiv \underline{D}(\underline{E}) \quad (21)$$

The vector quantities present in Maxwell's equations meet the following dependencies at environment boundaries:

$$\underline{n} \cdot (\underline{J}_1 - \underline{J}_2) = 0 \quad (22)$$

$$\underline{n} \cdot (\underline{B}_1 - \underline{B}_2) = 0 \quad (23)$$

$$\underline{n} \times (\underline{H}_1 - \underline{H}_2) = \underline{J}_s \quad (24)$$

$$\underline{n} \cdot (\underline{D}_1 - \underline{D}_2) = \rho_s \quad (25)$$

$$\underline{n} \times (\underline{E}_1 - \underline{E}_2) = 0 \quad (26)$$

In the case of numerical electromagnetic field calculations for low frequencies, Maxwell's equations are solved indirectly with the aid of a couple of potentials and boundary conditions. Where the potentials are given, the field vectors  $E$ ,  $D$ ,  $H$ ,  $B$ ,  $J$  can be determined.

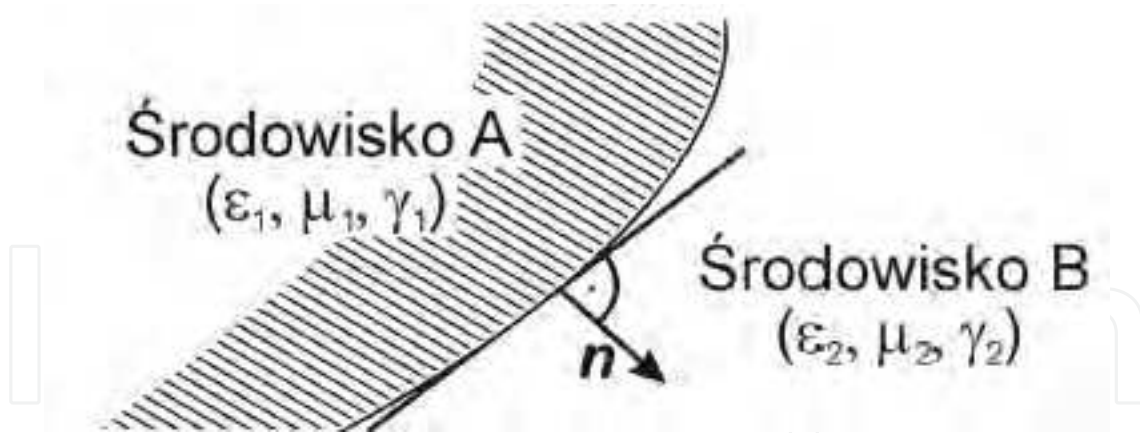


Fig. 19. Boundary of environments of diverse material properties

Maxwell's equations are most often solved by two types of potentials:

- Magnetic vector potential  $A$  ( $\underline{B} = \nabla \cdot \underline{A}, \nabla \cdot \underline{A} = 0$ ),
- Total magnetic scalar potential  $\Psi$  ( $\underline{H} = -\nabla \Psi$ ).

In the literature describe the vector of magnetic field intensity using a scalar potential function  $\Psi$ , expressed as:

$$\underline{H} = -\nabla \psi \quad (27)$$

When the material formula  $\underline{B} = \mu(\underline{H})\underline{H}$  and the condition of source-free magnetic field are taken into account, a differential equation of total magnetic scalar potential results:

$$\nabla \cdot (\mu \nabla \psi) = 0 \quad (28)$$

Where conduction currents appear, the vector of magnetic field intensity  $H$  includes two components:

$$\underline{H} = \underline{H}_s + \underline{H}_m \quad (29)$$

where:  $H_s$  - magnetic field intensity component enforced by flow of currents in a uniform environment,  $H_m$  - magnetic field intensity component arising from magnetisation of the environment material.

$H_s$  is computed according to Biot-Savart law as:

$$\underline{H}_s = \int \frac{\underline{J} \times \underline{1}_r}{4\pi r^2} dV \quad (30)$$

where:  $r$  is the distance from the observation point  $O=(x, y, z)$  where  $H_s$  is calculated to the source point  $Z=(x', y', z')$ .  $\underline{1}_r$  is a unit vector oriented from  $Z$  to  $O$ .

In addition,  $H_s$  in the area  $V$  fulfils the condition:

$$\nabla \times \underline{H}_s = \underline{J} \quad (31)$$



The following obtains for  $H_m$ :

$$\nabla \times \underline{H}_m = 0 \quad (32)$$

Expressing  $H_m$  as a function of magnetically reduced scalar potential  $\Phi$  results in:

$$\underline{H}_m = -\nabla\Phi \quad (33)$$

Based on (30) and (31), the magnetic intensity can be expressed:

$$\underline{H} = \frac{1}{\mu(\underline{B})} \underline{B} = \int \frac{\underline{J} \times \underline{1}_r}{4\pi r^2} dV - \nabla\Phi \quad (34)$$

Considering (14), (34) becomes:

$$\nabla \cdot (\mu \nabla \Phi) = \nabla \cdot (\mu \underline{H}_s) \quad (35)$$

The following material dependency is applied to models comprising a permanent magnet:

$$\underline{B} = \mu(\underline{H})(\underline{H} - \underline{H}_c) \quad (36)$$

Consequently, (35) describing the magnetically reduced scalar potential becomes:

$$\nabla \cdot (\mu \nabla \Phi) = \nabla \cdot (\mu \underline{H}_s) - \nabla \cdot (\mu \underline{H}_c) \quad (37)$$

In current-free areas, the resultant vector of magnetic field intensity  $H$  can only be described by means of the total magnetic potential.

$$\nabla \cdot (\mu \nabla \Psi) = \nabla \cdot (\mu \underline{H}_c) \quad (38)$$

Low accuracy of determining the magnetic field in the area of magnetic materials is the fundamental drawback of the reduced scalar potential method. This results from the fact that components of the magnetic field intensity vector  $H_s$  and  $H_m$  have similar values but opposite orientations. In effect, the resultant vector of intensity  $H$  reduces.

Where magnetic permeability  $\mu$  is high, great errors arise. To avoid the error in effect of the diminishing resultant vector of magnetic field intensity in numerical calculations, the area is divided into a sub-area  $V_\Phi$  of permeability  $\mu_0$  including current sources and a sub-area  $V_\Psi$  which includes the remaining area under consideration. Field distribution across  $V_\Psi$  is described by global scalar magnetic potential whereas  $V_\Phi$  is described by reduced scalar magnetic potential. To obtain a unique solution to (37) and (38), conditions present on boundaries of the different sub-areas described with the different types of scalar magnetic potential must be defined. This relates to the need to provide continuity of the normal component of magnetic induction vector and the tangential component of the magnetic field intensity vector on the boundary of  $V_\Psi$  and  $V_\Phi$ , which can be expressed:

$$\left( -\frac{\partial \Psi}{\partial t} \right)_{S_{\Phi-\Psi}} = \left( -\frac{\partial \Phi}{\partial t} + H_{st} \right)_{S_{\Phi-\Psi}} \quad (39)$$

where:

$S_{\Phi-\Psi}$  – boundary area between  $V_{\Psi}$  and  $V_{\Phi}$ ;  
 $H_{st}$  – active component of  $H_s$  on the area  $S_{\Phi-\Psi}$ .

One of the most commonly used numerical methods of solving field (boundary) problems is the Finite Element Method. Its idea is to divide an area under consideration into some discrete sub-areas of any shape (finite elements). The smaller the elements into which an analysed area is split, the more precise results of the calculations.

Triangular, quadrangular, six- or four-sided elements are those used most frequently. A four-sided element can serve to interpolate a given area (Figure 20) to produce the equations below (38):

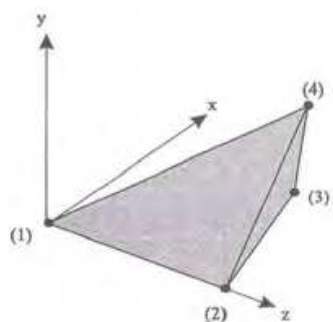


Fig. 20. Nodes of a sample four-sided element

$$\begin{bmatrix} u_1^e \\ u_2^e \\ u_3^e \\ u_4^e \end{bmatrix} = \begin{bmatrix} 1 & x_{11} & x_{21} & x_{31} \\ 1 & x_{12} & x_{22} & x_{32} \\ 1 & x_{13} & x_{23} & x_{33} \\ 1 & x_{14} & x_{24} & x_{34} \end{bmatrix} \begin{bmatrix} \beta_1 \\ \beta_2 \\ \beta_3 \\ \beta_4 \end{bmatrix} \tag{40}$$

where: e –element number,  $x_1, x_2, x_3$  – coordinates of a point inside the element,  $\beta_1, \beta_2, \beta_3, \beta_4$  - constants of an approximating function.

Solving this equation produces field values in the individual nodes. Figure 21 shows the most common discretisation shapes applied to 3D problems as part of FEM.

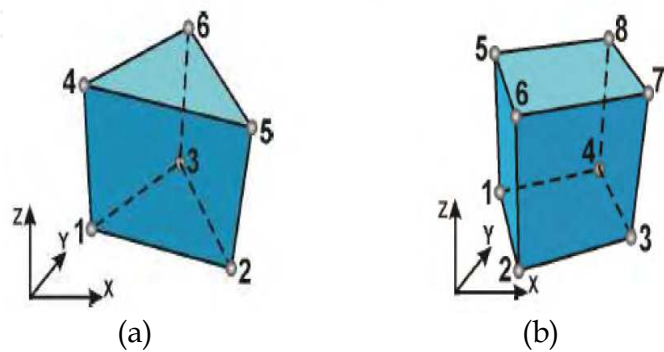


Fig. 21. Examples of three-dimensional elements utilised in FEM: a) five-sided element, b) six-sided element

Triangular three-node elements are most often used to discretise 2D areas. A sample division of  $\Omega$  of boundary  $\Gamma$  into triangular elements is illustrated in Figure 22.

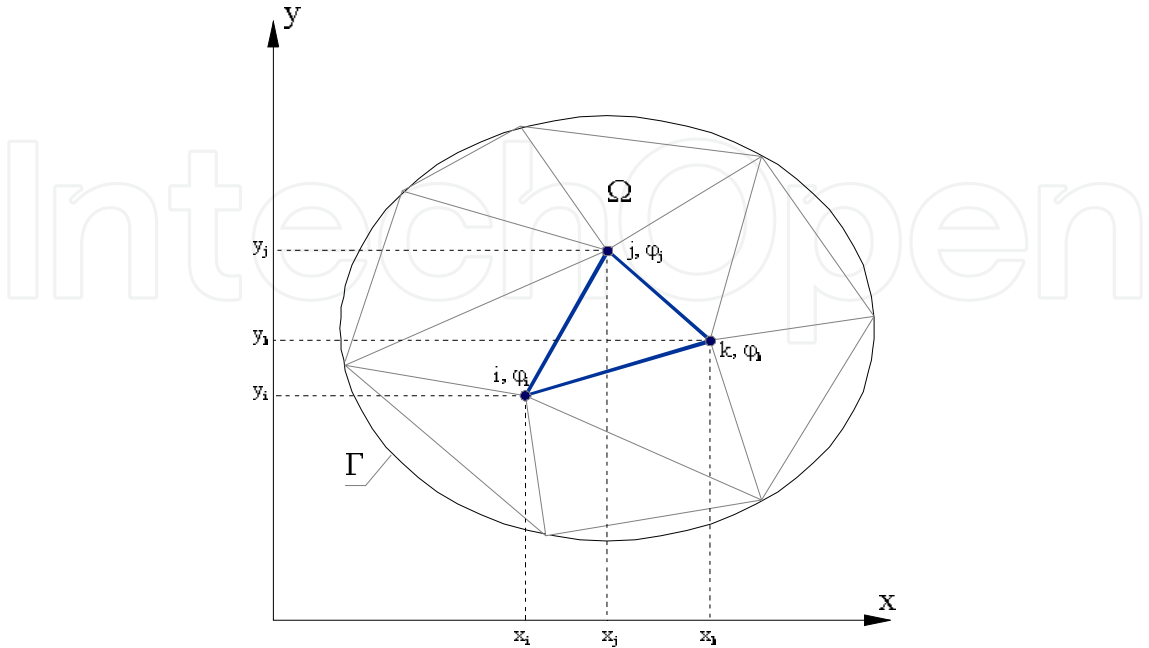


Fig. 22. Division of a two-dimensional area  $\Omega$  into triangular elements

Dependence of the sought quantity  $\varphi(x,y)$  inside the triangular element (e) is approximated by means of a first-degree polynomial:

$$\varphi^{(e)} = \alpha_1 + \alpha_2 \cdot x + \alpha_3 \cdot y$$

(41)

Values of  $\varphi(x,y)$  at nodes of e<sup>th</sup> element are described by a system of equations:

$$\begin{cases} \varphi_i^{(e)} = \alpha_1 + \alpha_2 \cdot x_i + \alpha_3 \cdot y_i \\ \varphi_j^{(e)} = \alpha_1 + \alpha_2 \cdot x_j + \alpha_3 \cdot y_j \\ \varphi_k^{(e)} = \alpha_1 + \alpha_2 \cdot x_k + \alpha_3 \cdot y_k \end{cases}$$

(42)

The system will solve for factors  $\alpha_1, \alpha_2, \alpha_3$ . Substituting them in (41) produces:

$$\varphi^{(e)} = \frac{(a_1 + b_1x + c_1y)\varphi_i + (a_j + b_jx + c_jy)\varphi_j + (a_k + b_kx + c_ky)\varphi_k}{2\Delta}$$

(43)

where:

$$a_i = x_jy_k - x_ky_j, \quad b_i = y_j - y_k, \quad c_i = x_k - x_j$$

(44)

$$2\Delta = \begin{vmatrix} 1 & x_i & y_i \\ 1 & x_j & y_j \\ 1 & x_k & y_k \end{vmatrix}$$

(45)

The remaining factors are obtained by cyclical shifting of the indices  $i, j, k$ . (43) can be expressed as a matrix:

$$\varphi^{(e)} = [N_i \quad N_j \quad N_k] \begin{bmatrix} \varphi_i \\ \varphi_j \\ \varphi_k \end{bmatrix} = \mathbf{N} \varphi \quad (46)$$

where:

$$N_{i,j,k} = \frac{a_{i,j,k} + b_{i,j,k}x + c_{i,j,k}y}{2\Delta} \quad (47)$$

$N_i, N_j, N_k$  are functions of variables  $x$  and  $y$ , referred to as *shape* or *base functions* while  $\mathbf{N}$  is a *shape function matrix*. (46) describes the value of  $\varphi^{(e)}$  above the surface of a single element (e) (three values of  $\varphi^{(e)}$  for nodes  $i, j$  and  $k$ ). Solving with the aid of the finite element method consists in finding values of  $\varphi$  in respect of all the nodes of  $\Omega$ .

$$\varphi = \begin{bmatrix} \varphi_1 \\ \varphi_2 \\ \vdots \\ \varphi_r \end{bmatrix} \quad (48)$$

where  $r$  is the number of discretisation network nodes. To this end, the functional  $J(\varphi)$  is minimised in relation to  $\varphi$ .

$$\frac{\partial J}{\partial \varphi} = \begin{bmatrix} \frac{\partial J}{\partial \varphi_1} \\ \frac{\partial J}{\partial \varphi_2} \\ \vdots \\ \frac{\partial J}{\partial \varphi_r} \end{bmatrix} = 0 \quad (49)$$

The energetic functional with regard to the fields described by Laplace equation including Dirichlet's or Neuman's boundary conditions becomes:

$$J(\varphi) = \frac{1}{2} \iint_{\Omega} [k_x \left(\frac{\partial \varphi}{\partial x}\right)^2 + k_y \left(\frac{\partial \varphi}{\partial y}\right)^2] dx dy + \int_{\Gamma} \varphi dl \quad (50)$$

where  $k_x$  and  $k_y$  are the material constants in the direction of  $x$  and  $y$  (e.g. magnetic or electric permeability) while  $l$  is the length of the arc along the boundary  $\Gamma$ . The principle of summing all elements of  $\Omega$  applied to the functional, therefore (49) can be formulated:

$$\frac{\partial J}{\partial \varphi} = \sum_{i=1}^s \frac{\partial J_i^{(e)}}{\partial \varphi} = 0 \quad (51)$$

where  $s$  is the number of all elements in the calculation area. Differentiating (50) with respect to the sought  $\varphi(x,y)$  results in:

$$\frac{\partial J^{(e)}}{\partial \varphi_m} = \iint_{\Omega^{(e)}} \left[ k_x \frac{\partial \varphi}{\partial x} \frac{\partial}{\partial \varphi_m} \left( \frac{\partial \varphi}{\partial x} \right) + k_y \frac{\partial \varphi}{\partial y} \frac{\partial}{\partial \varphi_m} \left( \frac{\partial \varphi}{\partial y} \right) \right] dx dy. \quad (52)$$

for values  $i, j$  and  $k$  of  $m$ . Taking (43) and (47) into consideration, the differential expressions in (52) can be found:

$$\begin{cases} \frac{\partial \varphi}{\partial x} = \begin{bmatrix} \frac{\partial N_i}{\partial x} & \frac{\partial N_j}{\partial x} & \frac{\partial N_k}{\partial x} \end{bmatrix} \cdot \begin{bmatrix} \varphi_i \\ \varphi_j \\ \varphi_k \end{bmatrix} \\ \frac{\partial \varphi}{\partial y} = \begin{bmatrix} \frac{\partial N_i}{\partial y} & \frac{\partial N_j}{\partial y} & \frac{\partial N_k}{\partial y} \end{bmatrix} \cdot \begin{bmatrix} \varphi_i \\ \varphi_j \\ \varphi_k \end{bmatrix} \\ \frac{\partial}{\partial \varphi_m} \left( \frac{\partial \varphi}{\partial x} \right) = \frac{\partial N_m}{\partial x} \\ \frac{\partial}{\partial \varphi_m} \left( \frac{\partial \varphi}{\partial y} \right) = \frac{\partial N_m}{\partial y} \end{cases} \quad (53)$$

Substituting (52) in (51) results in:

$$\frac{\partial J^{(e)}}{\partial \varphi} = \begin{bmatrix} \frac{\partial J^{(e)}}{\partial \varphi_i} \\ \frac{\partial J^{(e)}}{\partial \varphi_j} \\ \frac{\partial J^{(e)}}{\partial \varphi_k} \end{bmatrix} = \begin{bmatrix} h_{ii}^{(e)} & h_{ij}^{(e)} & h_{ik}^{(e)} \\ h_{ji}^{(e)} & h_{jj}^{(e)} & h_{jk}^{(e)} \\ h_{ki}^{(e)} & h_{kj}^{(e)} & h_{kk}^{(e)} \end{bmatrix} \cdot \begin{bmatrix} \varphi_i \\ \varphi_j \\ \varphi_k \end{bmatrix} = h^{(e)} \varphi^{(e)} \quad (54)$$

where:

$$h_{pq} = \iint_{\Omega^{(e)}} \left[ k_x \frac{\partial N_i}{\partial x} \frac{\partial N_j}{\partial x} + k_y \frac{\partial N_i}{\partial y} \frac{\partial N_j}{\partial y} \right] dx dy \quad (55)$$

for values  $i, j, k$  of  $p$  and  $q$ . The matrix  $h^{(e)}$  in (53) is called *element rigidity matrix* (the upper index '(e)' is a reference to an element) and specifies material properties. On appropriate transformations of (44), (45), and (48), the following can be said in respect of a triangular element:



$$h^{(e)} = \begin{bmatrix} k_x b_i b_i + k_y c_i c_i & k_x b_i b_j + k_y c_i c_j & k_x b_i b_k + k_y c_i c_k \\ k_x b_j b_i + k_y c_j c_i & k_x b_j b_j + k_y c_j c_j & k_x b_j b_k + k_y c_j c_k \\ k_x b_k b_i + k_y c_k c_i & k_x b_k b_j + k_y c_k c_j & k_x b_k b_k + k_y c_k c_k \end{bmatrix} \cdot \frac{1}{4\Delta}. \quad (56)$$

(51) describes a differential of functional  $J$  with respect to the variable  $\varphi(x,y)$  sought for (e). When components of (54) in  $s$  elements are summed according to:

$$H_{ij} = \sum_{k=1}^s h_{ij} \quad (57)$$

a differential of the functional can be expressed for the entire area:

$$\frac{\partial J_i}{\partial \varphi} = H\varphi = 0 \quad (58)$$

$H$  in (58) is known as a *condition* or *rigidity matrix*. This is a band square matrix of the dimension  $r$  and a band width lower than the matrix's dimension.

To introduce the node variables defined by means of Dirichlet's boundary conditions to (58), the equations describing nodes of known  $\varphi$  can be eliminated. This procedure can be troublesome, however, when computer calculation algorithms are created as it requires appropriate lines and columns to be removed from the rigidity matrix. Another method of introducing Dirichlet's conditions has been proposed by Payne and Irons. Elements of  $H$  diagonals relating to a specific boundary node must be multiplied by a great number (e.g.  $10^{15}$ ) and the resultant product must be entered in an appropriate position of the zero vector which forms the right-handed side of (58). This procedure is widely used as it is easy to programme and does not require many operations, thereby minimising the time and cost of the calculations.

To find an approximate solution to a problem using FEM, the objective function needs to be defined, most often as a minimum error of the solution, Galerkin's method is of use in solving non-linear problems. The best solution for an area  $V$  delimited with certain boundary conditions is zeroing of the weighted average residuum  $R = \bar{\zeta} - \zeta$ , where  $\zeta$  is the precise solution and  $\bar{\zeta}$  an approximate solution. A general solution according to Galerkin's method can be presented as:

$$\int_V w_i R dV = 0 \quad i = 1, 2, 3, \dots, m \quad (59)$$

where:  $w_i$  – tapering functions

According to the weighted residuum method, the tapering functions are those which interpolate an approximate distribution of the solution across the area under analysis  $V$ . Poisson's equation is the most commonly applied differential equation:

$$\frac{\partial}{\partial x} \left( v_x \frac{\partial \zeta}{\partial x} \right) + \frac{\partial}{\partial y} \left( v_y \frac{\partial \zeta}{\partial y} \right) + \frac{\partial}{\partial z} \left( v_z \frac{\partial \zeta}{\partial z} \right) = -f(x, y, z) \in V \quad (60)$$

where  $\zeta$  may represent both scalar and vectoral magnetic potential.

Vectoral magnetic potential  $A$  is the sought quantity in 2D problems involving magnetic field. Scalar potential  $\Psi$ - $\Phi$  is the sought quantity in 3D problems ( $A$  can also be determined in FLUX 3D). These solutions overcome the need to apply analytical methods to solving of complicated differential equations, which is occasionally time-consuming and complex. At the present stage of computer technology, introducing several or a dozen thousand unknowns instead of a mere few makes little difference. FEM is additionally popular when compared to other numerical methods since:

- choice of shapes (and dimensions) which will serve to discretise is unlimited,
- any boundaries of discretised shapes can be very precisely approximated with straight- or curving-line elements,
- any desirable accuracy of calculations (restrictions on analysis time) can be attained by varying element sizes,
- diverse boundary conditions can be defined,
- the method is universal and can help to solve electromagnetic, electrostatic, magnetic and heat-flow problems.

The need to analyse complex physical models requires application of numerical methods that provide approximate results. Such results are subject to errors, however, due to a range of factors, such as:

- differential equation errors,
- errors due to simplifying assumptions (e.g. ignoring certain properties of some phenomena).

In the literature<sup>17 18</sup> have discussed errors at the stage of problem solving (a central element of numerical calculations). These errors depend on the calculation method and are sources of distortions that may lead to misrepresentations of phenomena. Sources of errors as part of FEM include:

- interpolation errors;
- approximation errors generated when solutions are sought within a limited area;
- errors relating to discontinuity of an environment's physical parameters;
- errors in representations of structure (geometry);
- errors relating to rounding of node values.

Additionally, 3D problems are exposed to:

- errors arising at magnetic field boundaries described by means of different potentials;
- errors arising in ferromagnet areas described by means of reduced scalar potential.

A local error in a point of a model generated by FEM is inherently connected to the size of its elements surrounding a given point whereas it is only loosely related to average size of

---

<sup>17</sup>Leśniewska E. (1997). Zastosowanie symulacji pól elektromagnetycznych w projektowaniu przekładników

<sup>18</sup>Wincenciak S. (1998). Metody i algorytmy optymalizacji kształtu obiektów w polu elektromagnetycznym

elements in a space under consideration<sup>19 20</sup>. The latter type of errors are more significant and more difficult to eliminate in non-linear problems.

In the literature<sup>21 22 23 24 25</sup> have presented various examples of applying FEM to magnetic field calculations, explained problems of discretising models, and discussed detailed requirements of shape functions.

## 6. Simulation model of induction heating in flux 3D software

Based on laboratory research which determined electric and magnetic properties of a 60E1 rail, the internal rail structure was divided into areas of different properties. A fundamental magnetic model of a rail was created in this manner. Rail web and its edges are characterised by diverse material and magnetic properties. Magnetic properties of the remaining rail portions (e.g. centre) are identical. A 3D model on the basis of geometric dimensions given in Figure 7 is extended with areas in respect of which separate prime magnetising curves were obtained, evidence of structural differences generated by the rolling process. Figure 23 shows a rail divided into areas of varying magnetic properties, associated with appropriate characteristics (prime magnetising curves in the respective colours).

Figure 24 illustrates the way material properties of the individual rail areas are defined. 'Magnetic property' tab is selected, a curve type is chosen by means of 'Isotropic spline saturation', then specific values from the characteristic  $\mathbf{B}=\mathbf{f}(\mathbf{H})$  are input. The more points are defined, the more accurate description of a given area.

Figure 25 presents a 3D rail model including divisions into areas of varying magnetic properties. The Figure distinguishes head, web edges, and central part of a rail.

Construction of a grid for further field calculations was the next step. Flux 3D automatically creates and generates a calculation grid from among three sizes available in the programme. The grid may also be more or less dense. The denser a calculation grid, the more precise the field calculations. Too dense a grid considerably prolongs the calculation process, unfortunately. A selected grid type is then generated and imposed upon the model. Figures 26 and 27 show a calculation grid for a constructed rail model.

A numerical model of the rail, serving to simulate induction heating, is shown in Figure 18 including a complete calculation grid imposed and a heating wire near a web edge.

<sup>19</sup>Mendrela E., Łukaniszyn M., Macek-Kamińska K. (2002). *Tarczowe silniki prądu stałego z komutacją elektroniczną*

<sup>20</sup>Wróbel R. (2000). *Analiza wpływu parametrów obwodu magnetycznego i elektrycznego na pracę silnika tarczowego prądu stałego z magnesami trwałymi i elektronicznym komutatorem*

<sup>21</sup>Binns K.J., Lawrenson P.J., Trowbridge C.W. (1995). *The Analytical and Numerical Solution of Electric and Magnetic Fields*

<sup>22</sup>Bolkowski S., Stabrowski M., Skoczylas J., Sroka J., Sikora J., Wincenciak S. (1993). *Komputerowe metody analizy pola elektromagnetycznego*

<sup>23</sup>Gawrylczyk K.M. (2007). *Analiza wrażliwościowa pola elektromagnetycznego z użyciem metody elementów skończonych*

<sup>24</sup>Jianming J. (1993). *The finite element method in electromagnetic*

<sup>25</sup>Sikora R. (1997). *Teoria pola elektromagnetycznego*

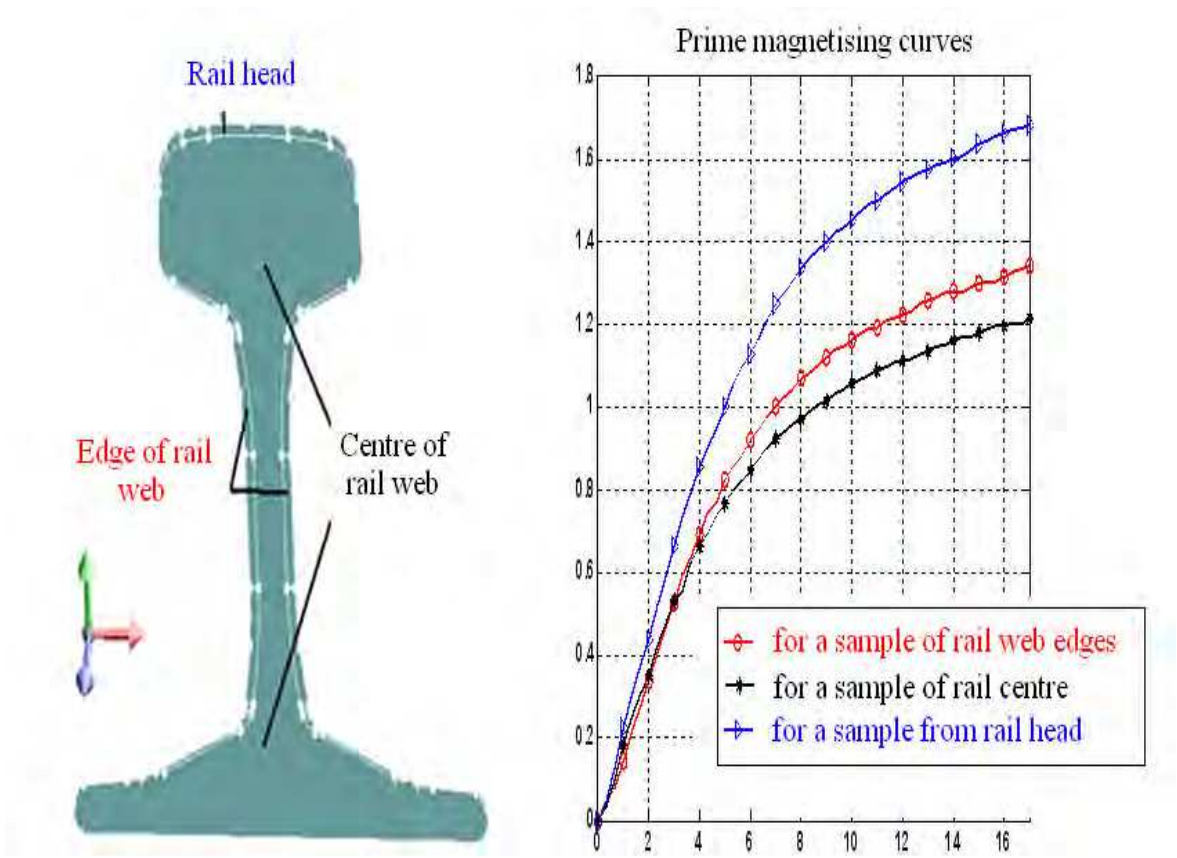


Fig. 23. Division of a rail into areas of varying magnetic properties, associated with appropriate characteristics (prime magnetising curves)

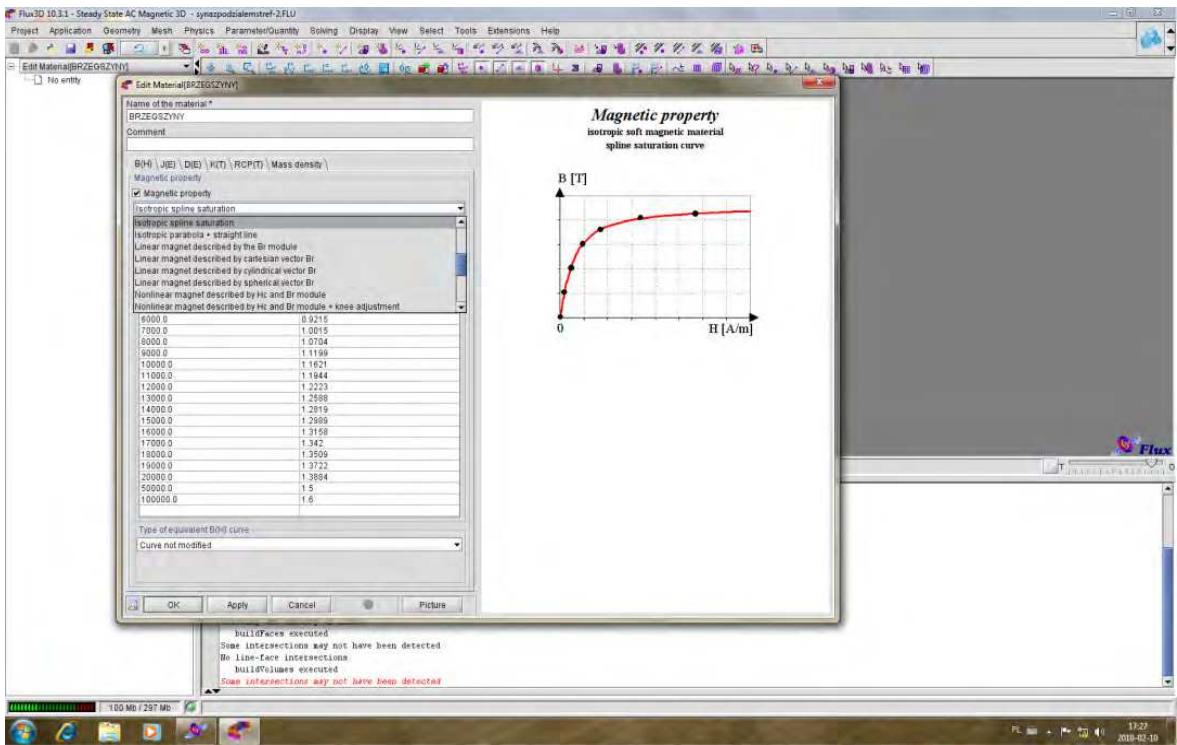


Fig. 24. Process of defining new materials and their magnetic properties



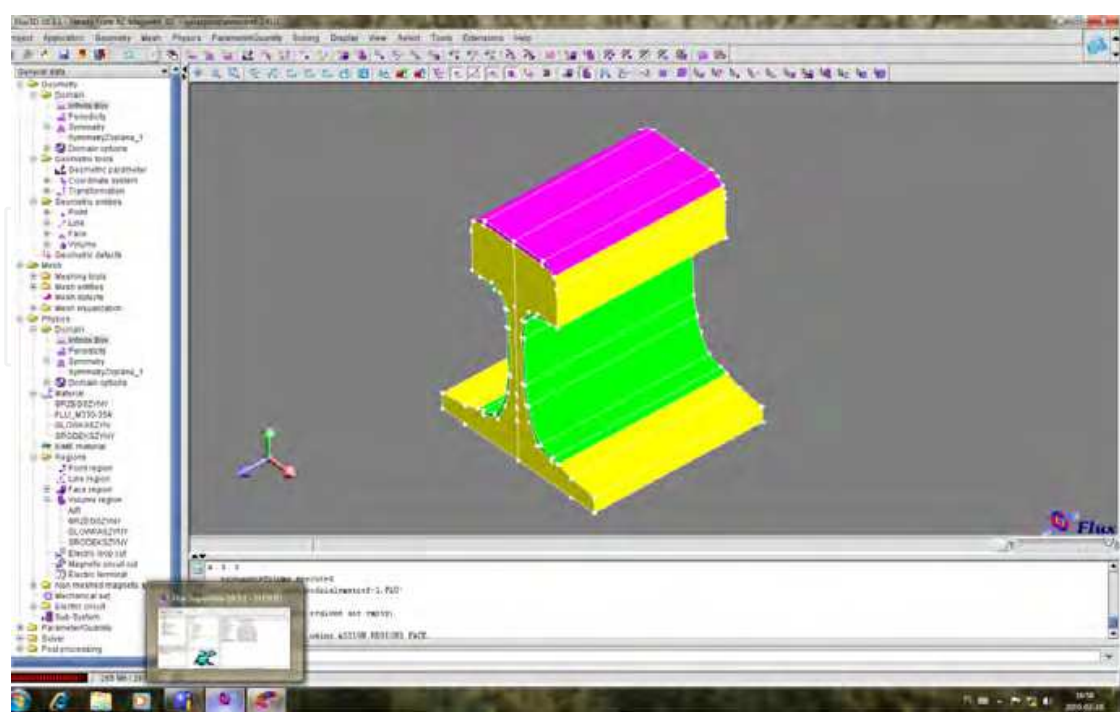


Fig. 25. Magnetic model of 60E1 rail in FLUX 3D software.

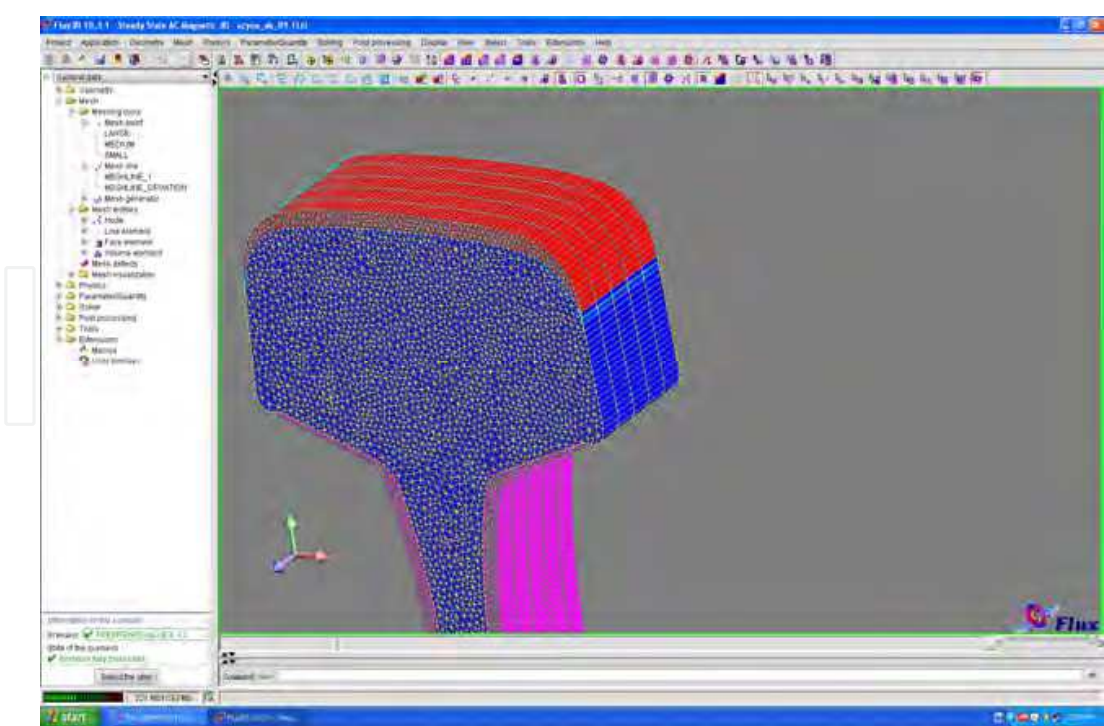


Fig. 26. Calculation grid for the rail head – red

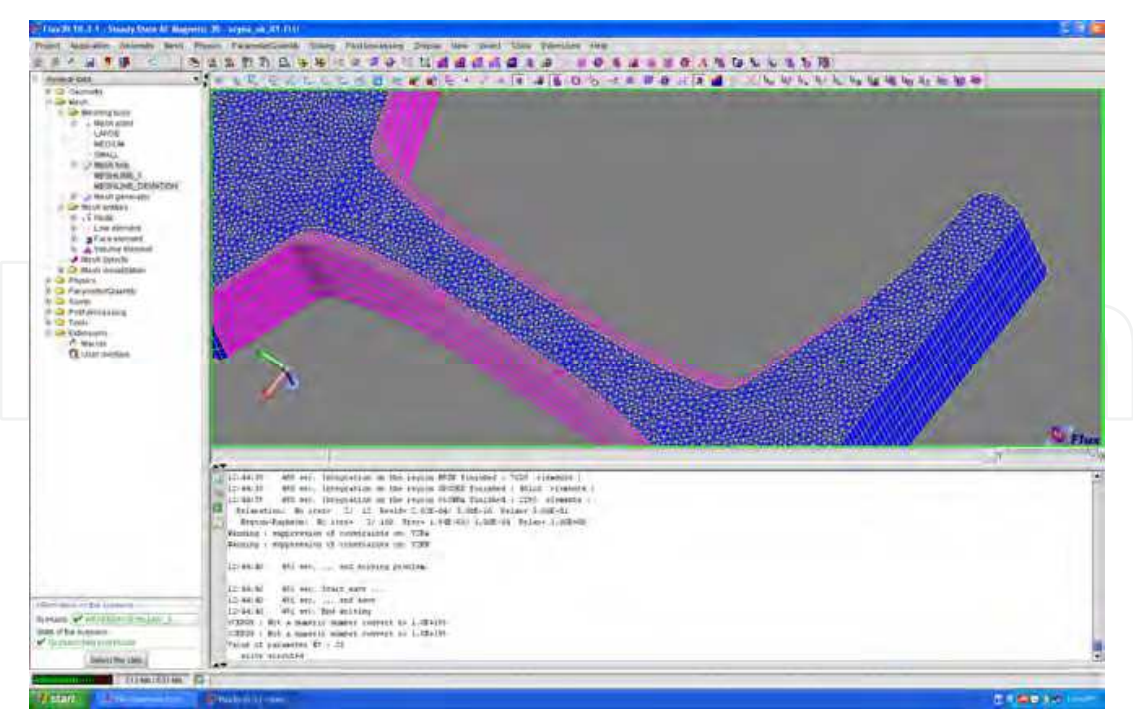


Fig. 27. A view of calculation grid executed in Flux 3D for rail web edges (pink) and rail centre (blue).

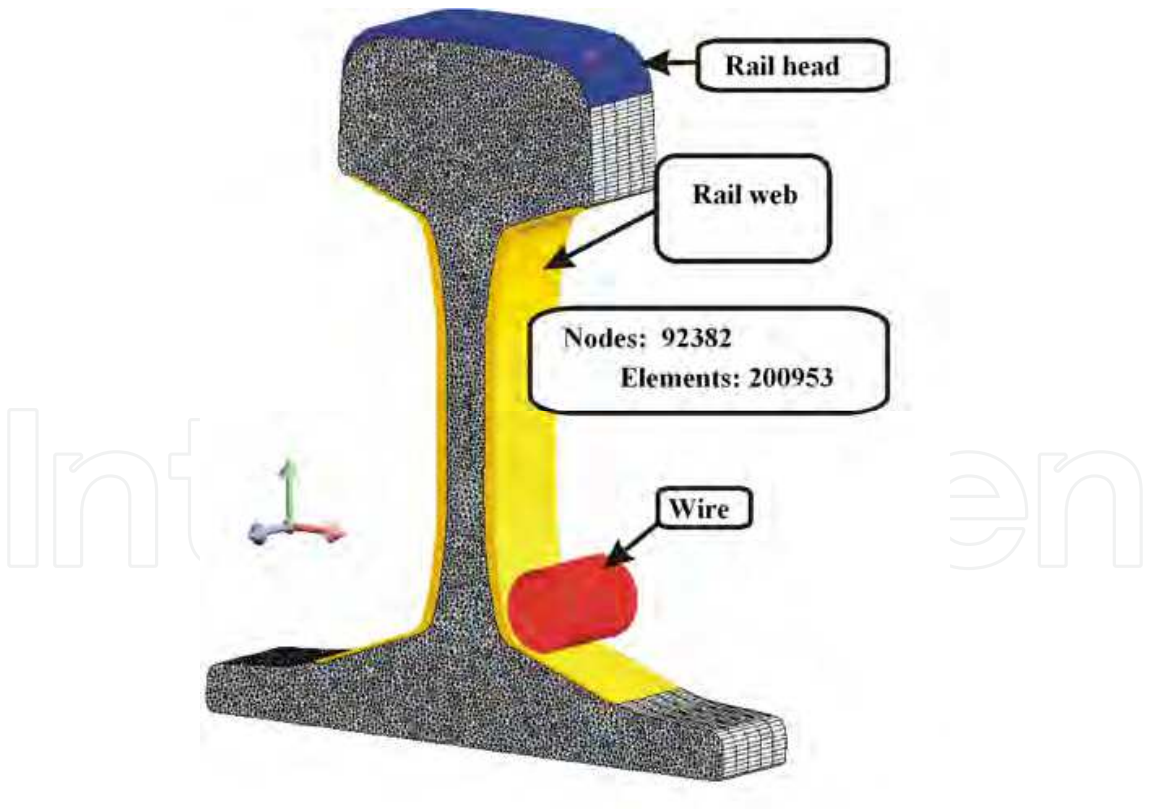


Fig. 28. Numerical model of the rail including a heating wire

This model is then subjected to the simulation process in order to determine behaviour of a rail when heated with eddy currents as part of induction heating.



The following assumptions underlie simulation testing of a rail at the time of induction heating in FLUX 3D software<sup>26 27</sup>:

- constant density of current across the heating wire,
- magnetic field description in 3D space with the aid of scalar magnetic potential,
- electric and magnetic parameters of a rail: electrical resistivity  $\rho$ , prime magnetising curve  $\mathbf{B} = f(\mathbf{H})$  or  $\mathbf{J} = f(\mathbf{H})$ , intensity of the coercion field  $\mathbf{H}_c$ , loss factors of eddy currents  $\mathbf{w}$  and of magnetic hysteresis loop  $\mathbf{h}$ ,
- zero boundary conditions:  $\mathbf{n} \cdot \mathbf{H} = 0$ .

The sample results were obtained in the simulation process at 650 Hz frequency and 11.14 MA/mm<sup>2</sup> density of the current across the wire. Set ranges of frequency and rms values of the current across the wire can be varied as part of this model.

Figure 29 presents a sample distribution of the absolute values of magnetic induction as obtained in the simulation process.

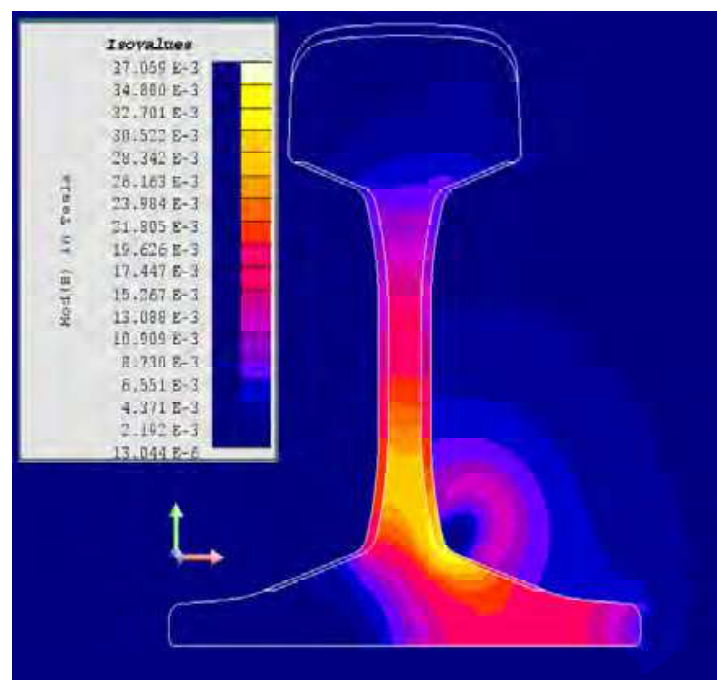


Fig. 29. Distribution of magnetic induction in the rail and its environment

Magnetic induction on the lateral web surface and on its foot reached a maximum of 0.037 T. This low value is due to the fact that an air gap appeared between the rail and the heating wire, impeding and dispersing the magnetic field. The wire itself was circular and its entire surface did not adhere to the rail, therefore magnetic field penetration into the rail was not effective.

Figure 30 shows the direction of magnetic field lines with regard to a rail placed inside the magnetic field of the heating wire.

<sup>26</sup>Femm, User's Manual, 2009

<sup>27</sup>Flux3d, User's guide, vol. 1-4, 2009

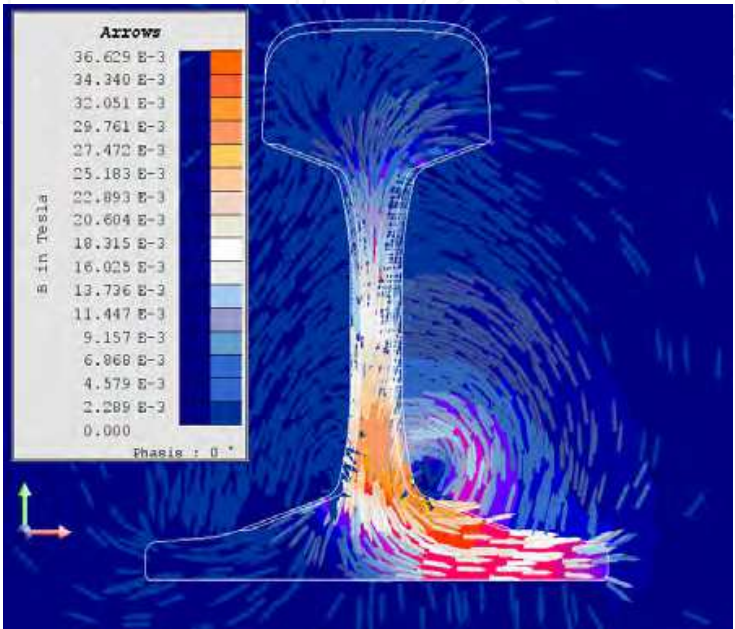


Fig. 30. Direction of magnetic field lines generated by the heating wire

This is the first model of induction heating of a rail forming part of a turnout to be developed by these authors. It was designed to demonstrate what phenomena occur when the rail is under the impact of a magnetic field. The rail and the wire do not form a full, closed magnetic loop. The magnetic field around the wire partly escapes into the air. As a result, penetration of the magnetic field into the rail structure is weaker and the magnetic induction on the rail surface is low. This weakened magnetic field may be insufficient to produce high eddy current densities in the rail and, in effect, it will be impossible to use induction heating for turnouts. Greater intensity of the magnetic field may improve the value of induction yet power losses associated with dispersion effects would increase.

Intensity of the magnetic field generated by the current across the coil is shown in Figure 31.

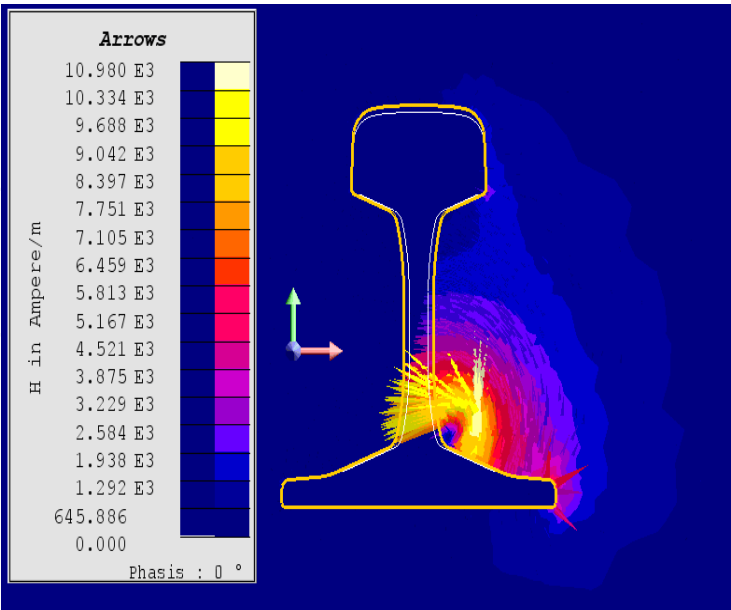


Fig. 31. Intensity of the magnetic field generated by the current across the heating wire

It is easy to read the value of magnetic field intensity arising from the heating wire: it approaches 11000A/m in the centre of the wire and reduces to 3000A/m at the contact of the rail and the wire after covering a distance of circa 1 centimetre (drag).

The air gap must be fully eliminated in continuing research and, should it prove impossible, the gap needs to be minimised in order to reduce magnetic field dispersion as much as practicable.

7. Conclusion

This chapter has presented elementary knowledge concerning 3D model illustrations of induction heating as applied to rail turnouts. It should be borne in mind, however, that a simulation model can differ widely from reality due, for instance, to simplifications discussed by the authors. The magnetic model itself must be modified in order to solve the issue of the air gap, for example.

It is also necessary to verify simulation results against those obtained in an actual model of turnout induction heating. Work on developing an actual model is in progress.

At the present stage, the magnetic model developed by the authors in Flux3D provides for observation of electric and magnetic effects in the rail’s internal structure triggered by flow of eddy currents. The model will be utilised to determine the depth of magnetic field penetration into the rail structure as dependent on variations of magnetising current frequency and will serve to determine a temperature distribution along the rail in the process of heating. Knowledge of this temperature distribution or, to be more exact, of maximum temperature values attained by the individual rail sections is the key to success of this research.

## 8. References

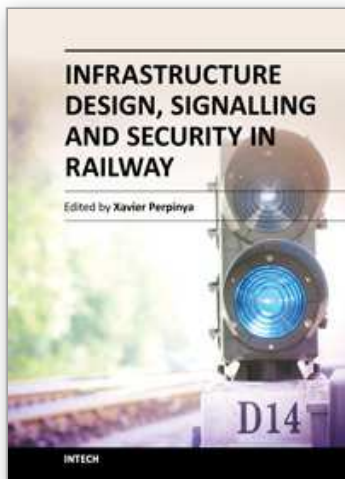
- Badania eksploatacyjne wodnego system ogrzewania rozjazdów typu MAS-Guben*, CNTK Warszawa, Styczeń 2004
- Binns K.J., Lawrenson P.J., Trowbridge C.W. (1995). *The Analytical and Numerical Solution of Electric and Magnetic Fields*, A Wiley-Interscience Publication, John Wiley & Sons, INC., New York
- Bolkowski S., Stabrowski M., Skoczylas J., Sroka J., Sikora J., Wincenciak S. (1993). *Komputerowe metody analizy pola elektromagnetycznego*, Wydawnictwo Naukowo – Techniczne, Warszawa
- Brodowski D., Andrulonis J. (2000). *Efektywność ogrzewania rozjazdów kolejowych*, CNTK, Warszawa
- Brodowski D., Andrulonis J. (2002). *Ogrzewanie rozjazdów kolejowych*, *Problemy kolejnictwa*, zeszyt 135, CNTK
- Femm, *User's Manual*, 2009
- Flux3d, *User's guide*, vol. 1-4, 2009
- Gawrylczyk K.M. (2007). *Analiza wrażliwościowa pola elektromagnetycznego z użyciem metody elementów skończonych*, Instytut Naukowo-Badawczy ZTUREK, Warszawa
- Gignoux D., Schlenker M. (2005). *Magnetism Fundamentals*, Springer, Grenoble
- Gozdecki T., Hering M., Łobodziński W. (1979). *Urządzenia elektroniczne. Elektroniczne urządzenia grzejne*, Wydawnictwa Szkolne i Pedagogiczne, Warszawa
- Grobelny M. (2009) *Budowa, modernizacja, naprawa i remonty nawierzchni kolejowej – urządzenia i elementy*, RYNEK KOLEJOWY, 2009-03-09
- Instrukcja eksploatacji i utrzymania urządzeń elektrycznego ogrzewania rozjazdów*, PKP Polskie Linie Kolejowe S.A., Warszawa, 2007
- Jianming J. (1993). *The finite element method in electromagnetic*, A Wiley-Interscience Publication, John Wiley & Sons, INC., New York
- Jiles D. (1991). *Introduction to Magnetism and Magnetic Materials*, Chapman & Hall, ISBN 0-412-386-30-5, New York
- Kiraga K., Szycha E., Andrulonis J. (2010). *Wybrane metody ogrzewania rozjazdów kolejowych – artykuł przeglądowy*, PRZEGLĄD ELEKTROTECHNICZNY, ISSN 0033-2097, R. 86 NR 2/2010
- Kuryłowicz J. (1962). *Badania materiałów magnetycznych*, Wydawnictwo Naukowo-Techniczne, Warszawa
- Leśniewska E. (1997). *Zastosowanie symulacji pól elektromagnetycznych w projektowaniu przekładników*, Zeszyty Naukowe Politechniki Łódzkiej, Nr 766, Łódź
- Materiały seminaryjne CNTK. (2004). *Wodne ogrzewanie rozjazdów kolejowych typu MAS*, Warszawa, 21-22 Kwiecień
- Mendrela E., Łukaniszyn M., Macek-Kamińska K. (2002). *Tarczowe silniki prądu stałego z komutacją elektroniczną*, Wydawnictwo Gnome, Katowice
- Praca zbiorowa: *Studium na temat wyboru optymalnego systemu ogrzewania rozjazdów*, COBiRTK, 1971
- Prospekt informacyjny o otulinach firmy Haet Point*, 2009.
- Sajdak Cz., Samek E. (1985). *Nagrzewanie indukcyjne. Podstawy teoretyczne i zastosowanie*, Wydawnictwo „Śląsk”, Katowice
- Sikora R. (1997). *Teoria pola elektromagnetycznego*, Wydawnictwo Naukowo-Techniczne, Warszawa

strona internetowa szyn: [www.inzynieria-kolejowa.dl.pl](http://www.inzynieria-kolejowa.dl.pl).

Wielgosz R. (2009). *Łączenie bezstykowych szyn kolejowych*, MECHANIKA CZASOPISMO TECHNICZNE, Wydawnictwo Politechniki Krakowskiej, 2-M/2009, Zeszyt 6, Rok 106.

Wincenciak S. (1998). *Metody i algorytmy optymalizacji kształtu obiektów w polu elektromagnetycznym*, Oficyna wydawnicza Politechniki Warszawskiej, Warszawa

Wróbel R. (2000). *Analiza wpływu parametrów obwodu magnetycznego i elektrycznego na pracę silnika tarczowego prądu stałego z magnesami trwałymi i elektronicznym komutatorem*, Rozprawa doktorska, Łódź



## **Infrastructure Design, Signalling and Security in Railway**

Edited by Dr. Xavier Perpinya

ISBN 978-953-51-0448-3

Hard cover, 522 pages

**Publisher** InTech

**Published online** 04, April, 2012

**Published in print edition** April, 2012

Railway transportation has become one of the main technological advances of our society. Since the first railway used to carry coal from a mine in Shropshire (England, 1600), a lot of efforts have been made to improve this transportation concept. One of its milestones was the invention and development of the steam locomotive, but commercial rail travels became practical two hundred years later. From these first attempts, railway infrastructures, signalling and security have evolved and become more complex than those performed in its earlier stages. This book will provide readers a comprehensive technical guide, covering these topics and presenting a brief overview of selected railway systems in the world. The objective of the book is to serve as a valuable reference for students, educators, scientists, faculty members, researchers, and engineers.

### **How to reference**

In order to correctly reference this scholarly work, feel free to copy and paste the following:

Elżbieta Szychta, Leszek Szychta, Mirosław Luft and Kamil Kiraga (2012). Application of 3D Simulation Methods to the Process of Induction Heating of Rail Turnouts, Infrastructure Design, Signalling and Security in Railway, Dr. Xavier Perpinya (Ed.), ISBN: 978-953-51-0448-3, InTech, Available from: <http://www.intechopen.com/books/infrastructure-design-signalling-and-security-in-railway/application-of-3d-simulation-methods-to-the-process-of-induction-heating-of-railroad-turnouts->

**INTECH**  
open science | open minds

### **InTech Europe**

University Campus STeP Ri  
Slavka Krautzeka 83/A  
51000 Rijeka, Croatia  
Phone: +385 (51) 770 447  
Fax: +385 (51) 686 166  
[www.intechopen.com](http://www.intechopen.com)

### **InTech China**

Unit 405, Office Block, Hotel Equatorial Shanghai  
No.65, Yan An Road (West), Shanghai, 200040, China  
中国上海市延安西路65号上海国际贵都大饭店办公楼405单元  
Phone: +86-21-62489820  
Fax: +86-21-62489821



© 2012 The Author(s). Licensee IntechOpen. This is an open access article distributed under the terms of the [Creative Commons Attribution 3.0 License](https://creativecommons.org/licenses/by/3.0/), which permits unrestricted use, distribution, and reproduction in any medium, provided the original work is properly cited.

IntechOpen

IntechOpen